Electromagnetic compatibility of a multimodal sensor front end for bioelectrical measurements

Joel Kattelus

School of Electrical Engineering

Thesis submitted for examination for the degree of Master of Science in Technology.

Espoo, July 26, 2021

Thesis supervisor:

Prof. Simo Särkkä

Thesis advisors:

D.Sc. (Tech.) Juha Virtanen

D.Sc. (Tech.) Kim Blomqvist

Aalto University
School of Electrical
Engineering

AALTO UNIVERSITY
SCHOOL OF ELECTRICAL ENGINEERING

ABSTRACT OF THE
MASTER'S THESIS

Author: Joel Kattelus

Title: Electromagnetic compatibility of a multimodal sensor front end for bioelectrical measurements

Date: July 26, 2021 Language: English Number of pages: 6+59

Department of Electrical Engineering and Automation

Professorship: Sensor informatics and medical technology

Supervisor: Prof. Simo Särkkä

Advisors: D.Sc. (Tech.) Juha Virtanen, D.Sc. (Tech.) Kim Blomqvist

Improving hospital workflows, patient safety and patient comfort are driving new solutions to clinical patient monitoring. Reduced size and weight of the instruments have already enabled monitoring in previously unmonitored areas, such as general wards.

This thesis studies electromagnetic compatibility (EMC) of a multimodal analog front end (AFE) component for vital signs monitoring. The AFE architecture features time-division multiplexing (TDM) for measuring electrocardiogram (ECG), impedance-based respiration rate (RR), and pulse oximetry within one unified architecture. The TDM architecture decreases the number of needed amplifiers, filters, and analog-to-digital converters within the chip, effectively reducing the size and therefore also the cost of the component. Reduced size and cost would be especially beneficial in disposable sensor patches.

To study the feasibility of the AFE, a wireless, battery-powered prototype of a combined ECG and RR sensor was developed. The prototype was tested against relevant EMC standards, with a focus on the electromagnetic immunity of the AFE.

The results show that the current design with unshielded electrode lead wires is highly susceptible to electromagnetic interference at certain resonant frequencies. It was not possible to reduce the level of interference to an acceptable level by adding passive filtering to the signal lines. However, no interference was observed when using shielded coaxial lead wires, excluding some corner cases with extremely high electric field strengths.

The thesis offers a thorough overview of the challenges with the tested design and indicates where to concentrate in future development. With shielded lead wires, the current design has the potential to pass the standard tests with minor modifications. The tested design would need substantial modifications in order to meet the EMC standard requirements with unshielded lead wires.

Keywords: electrocardiography, respiration rate, impedance plethysmography, disposable, body-worn, patient monitoring, continuous monitoring, electromagnetic immunity, standard testing

AALTO-YLIOPISTO
SÄHKÖTEKNIIKAN KORKEAKOULU

DIPLOMITYÖN
TIIVISTELMÄ

Tekijä: Joel Kattelus

Työn nimi: Multimodaalisen analogisen etuasteen elektromagneettinen yhteensopivuus biosähköisissä mittauksissa

Päivämäärä: 26. heinäkuuta 2021 Kieli: Englanti Sivumäärä: 6+59

Sähkötekniikan ja automaation laitos

Professuuri: Sensori-informatiikka ja lääketieteellinen tekniikka

Työn valvoja: Prof. Simo Särkkä

Työn ohjaaja: TkT Juha Virtanen, TkT Kim Blomqvist

Sairaaloiden työvaiheiden sekä potilasturvallisuuden ja -hyvinvoinnin parantaminen ajavat kliinisten potilasvalvontaratkaisujen kehitystä. Uudenlaiset kevyt ja pienikokoiset instrumentit ovat mahdollistaneet potilasvalvonnan myös ennen valvomattomilla alueilla kuten sairaalan vuodeosastoilla.

Tässä diplomityössä tutkitaan multimodaalisen analogisen etuasteen elektromagneettista yhteensopivuutta (EMC) vitaalielintoimintojen valvontaan. Etuasteen arkkitehtuuri mahdollistaa aikajakoisen kanavoinnin sydänsähkökäyrän, impedanssipohjaisen hengitystaajuuden sekä veren happisaturaation mittaamisen yhtenäisessä etuasteessa. Aikajakoinen kanavointi vähentää tarvittavien vahvistimien, suodattimien ja analogia-digitaalimuuntimien määrää sirussa, joka puolestaan pienentää komponentin kokoa ja siten lopulta myös sen hintaa. Pieni koko ja hinta on ehdottoman tärkeää kertakäyttöisissä iholle kiinnitettävissä sensoreissa.

Etuasteen soveltuvuuden tutkimusta varten kehitettiin langaton ja paristotoiminen sydänsähkökäyrää sekä hengitystaajuutta mittaavan sensorin prototyyppi. Prototyyppi testattiin relevantteja EMC-direktiivejä vastaan keskittyen etuasteen elektromagneettisen immuniteettiin.

Tulokset osoittavat, että nykyinen etuasteen kytkentä suojaamattomilla elektrodikaapeleilla on altis elektromagneettisille häiriöille tietyillä taajuusalueilla. Häiriön kytkeytyminen oli niin voimakasta, että edes etuasteeseen lisätyt passiiviset suodatuskomponentitkaaan eivät auttaneet alentamaan häiriön tasoa lähelle hyväksyttyä tasoa. Käyttämällä suojattuja elektrodikaapeleita häiriöt kuitenkin pystyttiin eliminoimaan täysin, lukuunottamatta muutamaa reunatapausta erittäin korkeilla sähkökentän voimakkuuksilla.

Tämä työ tarjoaa kattavan yleiskuvan olemassaolevista haasteista tutkitussa kytkennässä ja rajaa suuntaviivoja keskittymiseen tulevaisuuden kehitystyöhön. Käytettäessä suojattuja elektrodikaapeleita nykyinen etuasteen kytkentä voisi olla toteuttamiskelpoinen pienin muutoksin. Sen sijaan EMC-direktiivien vaatimusten täyttäminen suojaamattomilla elektrodikaapeleilla vaatii vielä paljon työtä.

Avainsanat: elektrokardiografia, hengitystaajuus, impedanssipletysmografia, kertakäyttöinen, puettava, potilasvalvonta, sähkömagneettinen yhteensopivuus, standardivaatimukset

Preface

This thesis is a culmination of my internship at GE Healthcare. Working and learning with an industry leader in developing new solutions that truly have an impact on the health and well-being of people has been a special privilege.

First, I want to thank my manager Timo Toivanen and the entire management of GE Healthcare Finland for making this thesis possible during these uncertain and challenging times. Thank you for the support, and for making sure I have the needed time and resources to succeed in this task.

A special thank you to my advisors Juha Virtanen and Kim Blomqvist for trusting me with this opportunity and patiently guiding me during the past nine months. Without the unparalleled knowledge and experience of Juha and Kim, this work simply would have not been possible. Juha and Kim spent countless hours introducing me to the topic at hand, and answering my questions whenever needed. It has been a pleasure to work with such seasoned professionals with an undisputed passion for what they do. Additionally, the importance of Kim's efforts for the software development work cannot be overstated. I would also like to thank my supervisor Prof. Simo Särkkä for the important insights and guidance throughout this work.

I want to express my gratitude to the engineers of Analog Devices, Inc., for supporting me and taking the time to answer a never-ending list of questions and ideas. Thank you also to my colleagues at GE Healthcare for all the support. I wish to further thank Janne Klemetti to whom I am sincerely grateful for guiding me throughout the EMC testing processes, and Ville Vartiovaara, who was my trusted source of information during the design phases of the prototype.

Finally, a sincere thank you to my friends and family for the support and encouragement on the thesis and otherwise.

Helsinki, July 26, 2021

Joel J. M. Kattelus

Contents

List of Acronyms

AC	alternating current
ADI	Analog Devices, Inc
AFE	analog front end
AHA	American heart association
BLE	Bluetooth low energy
BW	bandwidth
CMOS	complementary metal-oxide-semiconductor
CMRR	common-mode rejection ratio
ECG	electrocardiography
EMC	electromagnetic compatibility
EMI	electromagnetic interference
FIFO	first in first out
FPU	floating point unit
GPIO	general-purpose input/output
IC	integrated circuit
ICU	intensive care unit
IEC	International electrotechnical commission
IPG	impedance plethysmography
JTAG	Joint Test Action Group
LED	light emitting diode
PCBA	printed circuit board assembly
RF	radio frequency
RLD	right leg drive
RR	respiration rate
SLIP	serial line internet protocol
SNR	signal-to-noise ratio
SPI	serial peripheral interface
TDM	time-division multiplexing
TIA	transimpedance amplifier

1 Introduction

In recent years, the miniaturization of technology has advanced the development of small form factor devices for a wide variety of medical instrumentation applications. One of these applications is in the vital signs monitoring of hospital patients. Vital signs monitoring has slowly shifted from traditional wired bedside monitoring to compact, wireless and wearable solutions.

Current state-of-the-art vital signs monitoring systems consist of sensors equipped with batteries transmitting the data using wireless technology to a centralized monitoring network. Wireless patient monitoring has increased patient comfort and enabled monitoring in previously unmonitored areas, such as general wards. Additionally, the ongoing COVID-19 pandemic has rapidly increased the global demand for monitoring and monitoring equipment (GE Healthcare, 2020) and increased interest in smart continuous monitoring solutions. The pandemic era has also further emphasized the importance of maintaining high standards of hygiene in a hospital environment, where the contamination of the care equipment is likely (Duan, Gao, and Wang, 2020; Coccolini et al., 2020; Wong et al., 2020).

A promising approach for alleviating the infection control challenge and streamlining the evolution to continuous monitoring has been introducing fully disposable sensors. To this day, disposable sensors have been limited to electrodes and passive probes with no active components or any kind of data processing capabilities. The new type of disposable sensors would include the same functionality as the reusable wireless alternatives with an even smaller and lighter form factor. Disposable sensors connected to the existing monitoring systems could eliminate the need for cleaning and disinfecting the sensors after each use. Furthermore, disposable sensors would eliminate the need for changing the batteries and any other maintenance tasks, freeing valuable time resources for nurses and care personnel. Finally, fully disposable sensors could further increase patient comfort by shifting away from clumsier and bulkier reusable solutions.

Currently, numerous vital signs sensing solutions with disposable features exist, but solutions for patient monitoring that are compliant with IEC60601-2-27 or IEC80601-2-49 standard requirements still remain uncommon. There are solutions such as Philips BX100 and Sensium® (Philips, 2021; Sensium Healthcare Ltd., 2020) that offer disposable patches specifically designed for ambulatory patient monitoring. However, a fully disposable solution that could deliver at least one standard lead electrocardiogram (ECG) and dual vector impedance respiration rate (RR) with apnea detection is yet to been developed. In order to transform the current reusable wireless patient monitoring sensors to fully disposable variants, a significant cost and size reduction to the design is required.

A partial solution for these challenges could be integrating multiple measurements to a single sensor front end chip, resulting in a dual- or multi-parameter front end. Integrating more than one measurement to one front-end would effectively reduce the size and cost of the sensor. Sensor front-end is responsible for creating and acquiring the measurement signals and is an essential component of any measurement device. Recently released ADPD4100 (ADI Analog Devices, Inc., Wilmington, MA, U.S.)

integrated circuit (IC) measures up to eight single-ended inputs with dual-channel simultaneous sampling (Analog Devices, Inc., 2020). The commissioner of this thesis, GE Healthcare Finland Oy has worked closely with ADI to test and evaluate the feasibility of the ADPD4100 for bioelectronic measurements. The new ADI sensor front-end enables time-division multiplexing for ECG and impedance plethysmogram (IPG) measurements, of which the latter is used to estimate respiration rate (RR). Conventional solutions usually continuously acquire the signals in dedicated frequency domains. Before this thesis, the feasibility of the new measurement principle has been demonstrated at GE Healthcare with bench top prototypes and signal simulators for ECG and RR. However, its capability to pass standards verification has been unknown.

Measuring weak biosignals is challenging as it is but becomes even more challenging when introduced into the real clinical environment, with noise sources ranging from power line noise to various electronic devices in hospitals. Measurement cables are great antennas for electromagnetic noise, which can lead to noise coupling to the measurement itself. This type of noise is called electromagnetic interference (EMI). An ideal sensor would be immune to any noise or interference present in the environment.

The new measurement principle introduces a challenge regarding the electromagnetic compatibility (EMC), interference sensitivity, and the intensity of the noise coupling to the novel sensor front-end in real-life clinical settings. Previous experience on the bio-electric sensors noise characteristics in clinical settings is based on studies with traditional wired bedside monitors, which do not directly apply to small form factor wireless and wearable equipment. It is also unknown how much this kind of novel measurement principle would benefit from using shielded lead wires instead of a more cost-friendly unshielded alternative.

Therefore, the aim of this thesis is to evaluate the feasibility of the ADPD4100 multimodal analog front end for ECG and RR sensing applications specifically considering the electromagnetic immunity of the sensor front-end. To achieve this purpose, a dual-parameter prototype of an ECG and RR sensor is developed based on the ADPD4100. The prototype is then subjected to a series of standard defined EMC tests while comparing the essential noise performance of the measurement front end. Additionally, the EMI performance of the design is evaluated with both unshielded and shielded lead wires with several passive input filtering configurations.

This thesis is structured as follows. Chapter 2 explores the theory and literature behind RR and ECG measurements and explores electromagnetic interference (EMI) and standard requirements. Chapter 3 describes the design and operation of the dual-parameter sensor prototype and the methodology for the conducted EMI tests. Chapter 4 presents the results of the EMC tests. Chapter 5 concludes the thesis by discussing the findings and proposes a direction for future work.

2 Background

For a thorough discussion of electromagnetic compatibility measurements conducted in this thesis, relevant measurement principles and basic electromagnetic noise characteristics are introduced in this chapter. This includes describing the concepts of the RR and ECG measurements in current state-of-the-art approaches. In addition, relevant background for electromagnetic interference together with standard requirements are discussed.

2.1 Respiration rate monitoring

The function of a respiration system is to exchange oxygen and carbon dioxide in and out of the bloodstream (Tortora and Derrickson, 2017). The muscles associated with lung inflation and deflation sequentially contract and relax, resulting in ventilation of the lungs, also known as breathing. Respiration rate (RR) is one of the four main vital signs (body temperature, blood pressure, heart rate, respiration rate) routinely monitored by medical professionals (Elliott and Coventry, 2012). RR reports how many times a patient breathes in a minute. Typically, a healthy human breathes 12–20 times a minute, one breath containing approximately 500 ml of air. For more information about the physiology and anatomy of the respiratory system, see, for example, Tortora and Derrickson (2017, pp. 850–897).

Generally, RR is monitored in the intensive care unit (ICU) or at acute care wards. However, RR is known as a significant predictor of patient deterioration (Vincent et al., 2018; Bunkenborg et al., 2019), leading to an increased interest for respiratory monitoring as well in hospital general care floors and postoperative care (McBride et al., 2005; Armitage, Eddleston, and Stokes, 2007; Ryan, Cadman, and Hann, 2004). For example, a study by Fieselmann et al. (1993) identified that RR of over 27 breaths per minute can predict a cardiopulmonary arrest for internal medicine inpatients. Still, RR is frequently omitted in patient monitoring (Kelly, 2018; Cretikos et al., 2008).

RR can be monitored by numerous techniques, as can be seen from the review by Al-Khalidi et al. (2011), where different technologies and techniques for respiratory analysis are presented. Respiration gases can be measured from intubated patients with capnography, involving sensors and equipment directly fitted to the invasive gas tubes (Gravenstein et al., 2011). Spirometry monitors the breath volume and airflow and is often used for diagnosing pulmonary conditions such as asthma or fibrosis (Thompson, O'Hehir, and Borg, 2014). Spirometry is generally viewed as a gold standard of respiratory monitoring, but due to its intrusive nature (requiring a face mask and a nose clip) it is not a desirable choice for continuous ambulatory monitoring (Młyńczak and Cybulski, 2012). Non-invasive methods for respiration monitoring include plethysmorgraphic pulse oximetry which can be used to derive the RR from the oxygen concentration of blood and blood flow fluctuation (Bergese et al., 2017). There are also acoustic and electromechanical measurement methods such as acoustic respiration rate (Ramsay et al., 2013) and respiratory inductive plethysmography (Retory et al., 2016). More modern approach includes utilizing accelerometer data

for detecting the breathing patterns based on the movement of thorax (Bates et al., 2010). While there are many respiratory measurement techniques available with certain benefits and drawbacks, a technology called impedance plethysmography (IPG) has been the most widely adopted method for periodic observation of RR in current patient monitors (Wilkinson and Thanawala, 2009; Wheatley, 2018).

2.1.1 Impedance plethysmography

Impedance plethysmography (IPG) measures the thoracic impedance change associated with respiration. The measurement utilizes a number of ECG electrodes placed across the patient's upper body. The body impedance is measured by supplying a small, usually less than 100 μA alternating current (AC) through the electrodes to the body, while simultaneously measuring the voltage change associated with impedance change produced by the movement of the thorax. During the breathing cycle, the inflation and deflation of the lungs cause the chest cavity to rise and fall. During inhalation, the skin stretches and contracts on the chest. This causes the electrical conductivity of the thorax to change. During expiration, the thorax conductivity again changes as the chest cavity falls and the skin relaxes. The phenomenon is described in more detail in the book by Malmivuo and Plonsey (1995). These changes in thorax conductivity produce measurable variations in thorax impedance which can be detected in the measurement.

Another take on the principle is that when the chest expands, the distance between the measuring electrodes increases, causing the impedance between the electrodes to increase (e.g. B. H. Brown et al., 1994). Additionally, the conductivity of lung tissue changes depending on the aeration level. The total impedance variation is subject to chest movement, distance change, and lung aeration level. The underlying physiological factors affecting the thoracic impedance change during respiration were a subject of interest already in the 1960s when Baker et al. (1966) studied the contribution of the thoracic cage movement to the impedance. Later in 1996, a study by Adler, Guardo, and Berthiaume (1996) identified that the movement of the rib cage and chest expansion accounts for up to 20% of the resulting impedance change.

IPG can be measured in either bipolar or tetrapolar configuration. In a bipolar configuration, the current injection electrodes are also used to simultaneously sense the corresponding voltage produced by thoracic impedance changes. The concept of bipolar IPG is described in Figure 1. The advantage of bipolar configuration is in its simplicity as it requires only two electrodes instead of four. However, the bipolar method is much more vulnerable for motion artifacts than the tetrapolar method, and it is difficult to separate the desired signal from the multitude of different impedance components (Młyńczak and Cybulski, 2012).

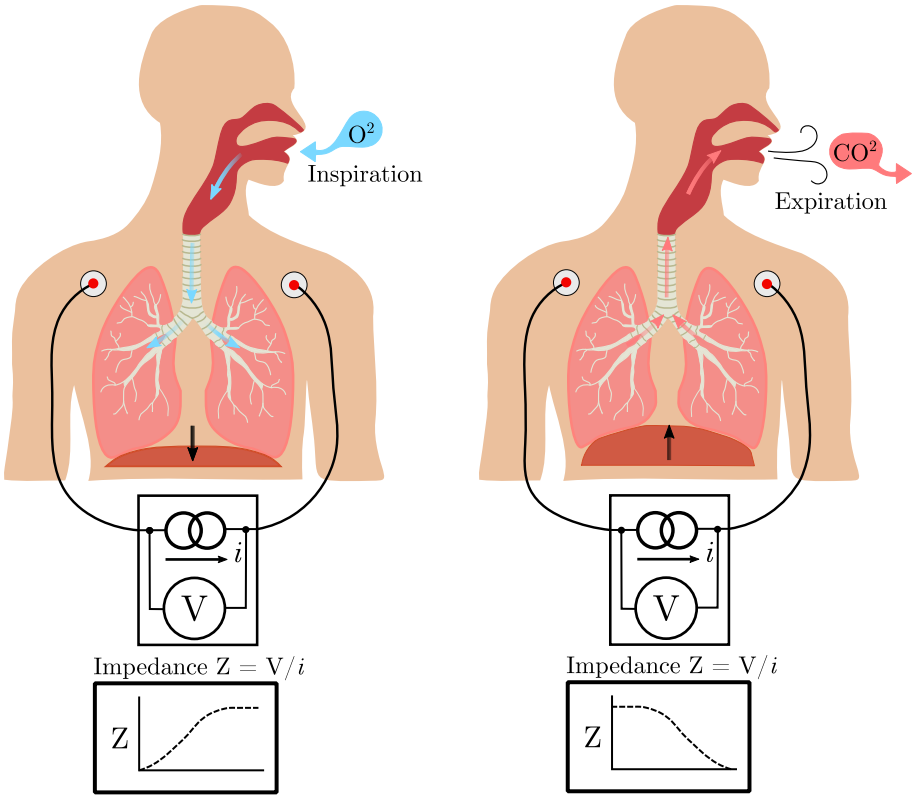

Figure 1: A model describing the effect of respiration to the IPG measurement in bipolar configuration.

Tetrapolar electrode configuration solves the problem by dividing the tasks of current injection and voltage sensing into two separate electrode pairs. The first pair is utilized for driving the injection current and the second is sensing the voltage. Tetrapolar IPG configuration is shown in Figure 2. In the tetrapolar configuration, as the electrodes are physically separated, the current is distributed more effectively, and the sensed voltage does not have an effect on the impedance of each electrode and surrounding skin and body tissue. It is possible to select the area of interest for voltage sensing even if the current is driven to the body elsewhere.

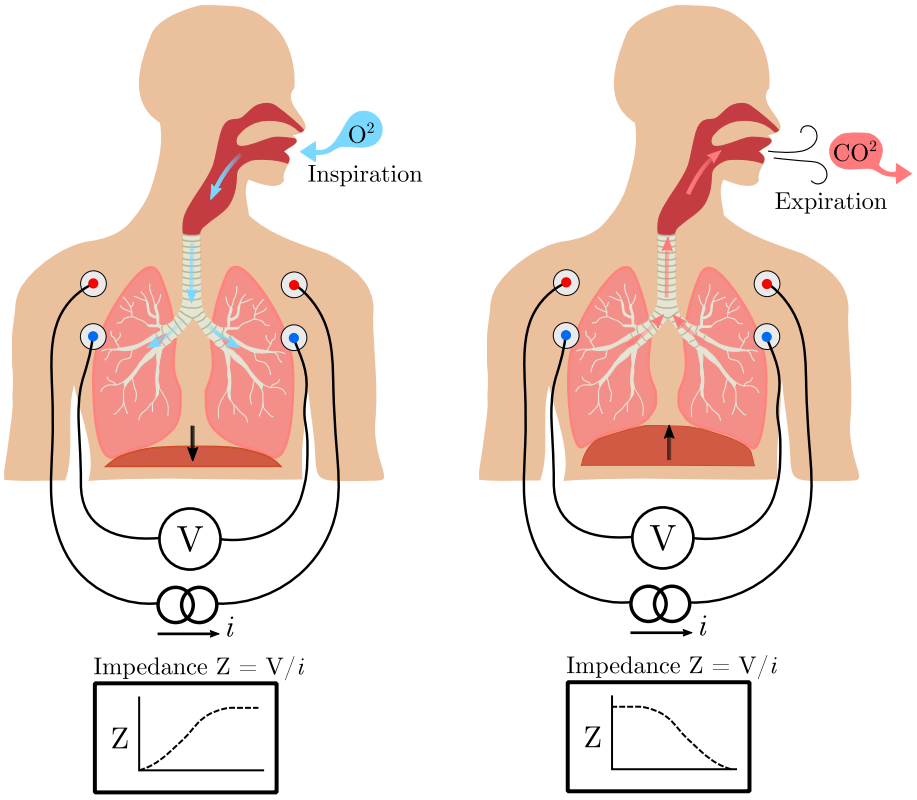

Figure 2: A model describing the effect of respiration to the IPG measurement in tetrapolar configuration.

There are also improved versions for both bipolar and tetrapolar methods including special guard circuits with amplifiers, but these are not used that often due to the increased complexity. However, the bipolar method is still a feasible option when properly designed. With help of algorithms and filtering, it is still a relevant method of measuring RR in clinical patient monitoring.

Characteristics of body impedance

Electrical impedance is a measure of the opposition or resistance in a circuit to time-varying electric current. In order to measure the body impedance, an electric current with a frequency scale of 10–100 kHz is introduced into the body while the corresponding voltage is measured across the thorax. The impedance Z is then calculated by dividing the voltage by the injected current. The resulting values are filtered and sampled in real-time and plotted into the monitor screen. Figure 3 shows a generalized view of the IPG measurement graph on a patient monitor.

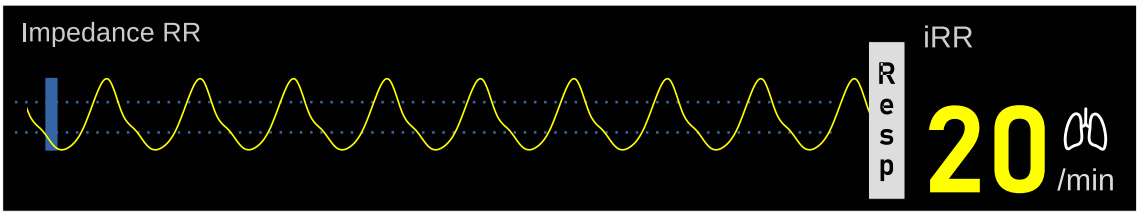

Figure 3: An example of respiration rate graph seen on a clinical patient monitor screen during the monitoring. The calculated respiration rate is visible on the right hand side, with the real-time plot of the impedance on the left hand side of the figure.

The impedance of a human body consists of numerous different tissues and their interfaces. Each tissue has its own unique cell structure and fluid concentration. Even within the same tissue, the cells vary in size, shape, and position due to their heterogeneous nature. These variables have a significant role in defining the total electrical conductivity of the human body.

In a tetrapolar IPG measurement, the direct impedance changes associated with breathing are only a fraction of the total body impedance. The measurement current travels through the electrodes, skin, and various different tissues, in which lungs are only a small part of the final equation. Carefully selected electrode locations together with the highly sensitive measurement help to maximize the acquired signal amplitude.

In a 12-subject study by B. H. Brown et al., 1994, a mean impedance change of 1-2 Ω was measured across the thorax during respiration. In the same study, it was also identified that the measured impedance amplitude decreases as the measurement frequency increases. In other words, the electrical conductivity σ (S/m) of the tissue is dependent on the measurement frequency f (Hz). Therefore, by optimizing also the measurement frequency, the subtle changes in impedance can be sensed with maximum precision.

Figure 4, combined according to the measurements of S. Gabriel, Lau, and C. Gabriel, 1996, presents the electrical conductivities of some tissues as a function of frequency. The plot shows that the conductivity of the skin is highly depended on the frequency, especially at below 10^7 Hz. Therefore, the impedance of the skin and especially the electrode-skin impedance has a considerable role in the measured total impedance. The conductivity of skin has the most variation within the presented frequency range as opposed to organs such as the spleen and liver, which have relatively high conductivity due to their high electrolyte content. The conductivity of lung tissue sits somewhere between muscle tissue and the liver. According to Grimnes and Martinsen, 2015 and Ackmann and Seitz, 1984, at frequencies below 10 kHz, the skin impedance is dominated by the keratin-lipid layer called the stratum corneum, which is the outermost layer of the skin (epidermis). The stratum corneum consists of dead and dry tissue and is generally a bad conductor. With frequencies above 10 kHz, the second outermost layer of the skin called the viable epidermis accounts for most of the impedance. Additionally, skin hydration and electrode size, geometry, and material have an important role in the entirety. In essence, higher measurement frequency leads to measurements at deeper layers in the skin. To improve SC contact

impedance, the electrodes often incorporate an electrolytic solution or wet gel.

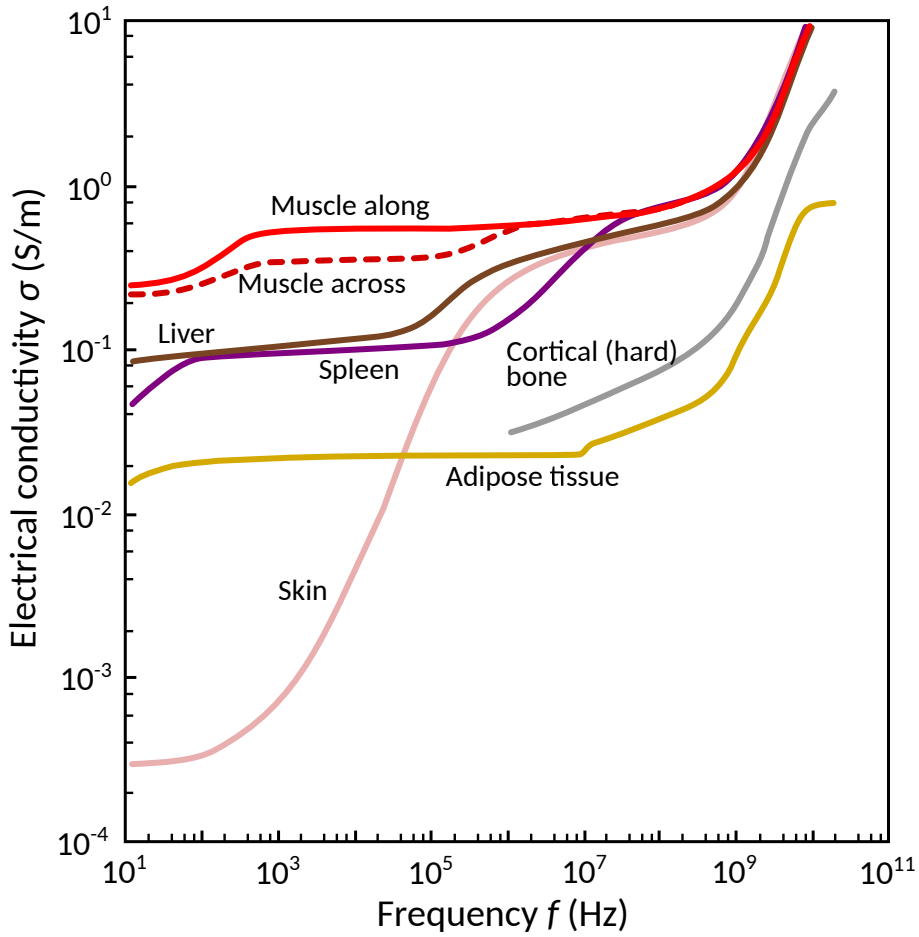

Figure 4: Compilation of electrical conductivities of different tissues as a function of frequency from 10 Hz to 100 GHz. Courtesy of Kim Blomqvist. Redrawn by K. Blomqvist on the basis of figures in S. Gabriel, Lau, and C. Gabriel (1996).

Electrode and lead configurations

As with most measurement methods, there are also drawbacks associated with IPG. It is highly sensitive to movement, which can cause movement artefacts to the measurement. Movement of the patient and especially the skin creates new pathways for the electrical currents making changes to the impedance. The effects of movement can be reduced by increasing the number of electrodes (tetrapolar method), or by developing measurement algorithms that can help to differentiate the real breathing pattern from the noise. Additionally, speech, posture, and physical activity present a much larger problem to the measurement of respiration than they do to cardiovascular recordings (Houtveen, Groot, and Geus, 2006). The positioning of the patient also highly affects the acquired respiration signal. If the patient is lying down, the breathing tends to be in the abdomen area, whereas if the patient is standing or sitting, breathing usually happens in the upper chest. Two vector

measurement setup tries to solve this issue by including two transverse planes to achieve at least one channel of good quality respiration signal. However, an additional electrode can be used in order to achieve satisfactory measurement results in both upright and lying positions. This allows for simultaneous measurement across the chest electrodes (lead I in Figure 5) and through the abdomen or left leg electrode (lead II in Figure 5).

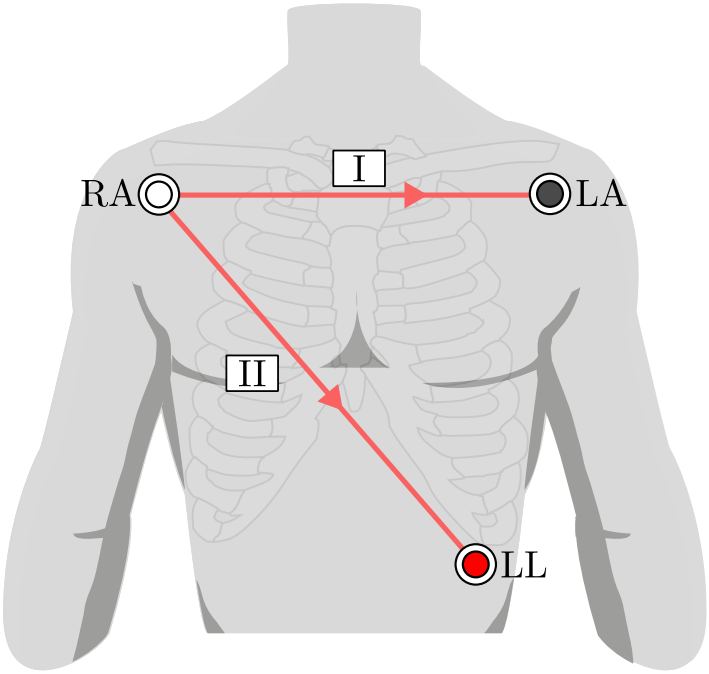

Lead	Composition
I	RA – LA
II	RA – LL

Figure 5: Common electrode locations for bipolar IPG measurement covering both transthoracic and transdiaphragmatic planes of the body. Redrawn from Redmond (2013) by author.

The current state-of-the-art IPG sensors utilize an instrumentation amplifier with an input filtering circuit for measuring the voltage from the patient's skin. The current is driven from digital or analog output pins of the AFE. Figure 6 shows a high-level block diagram of one channel IPG sensor front-end. Both IPG current drive and instrumentation amplifier input is isolated from the patient's body with defibrillator protection resistors. The current is fed through the resistors to the body while the voltage is simultaneously measured by the instrumentation amplifier. For two-channel measurement, an additional amplifier is added to the configuration with a dedicated current drive for the additional electrode, preferably at a different frequency.

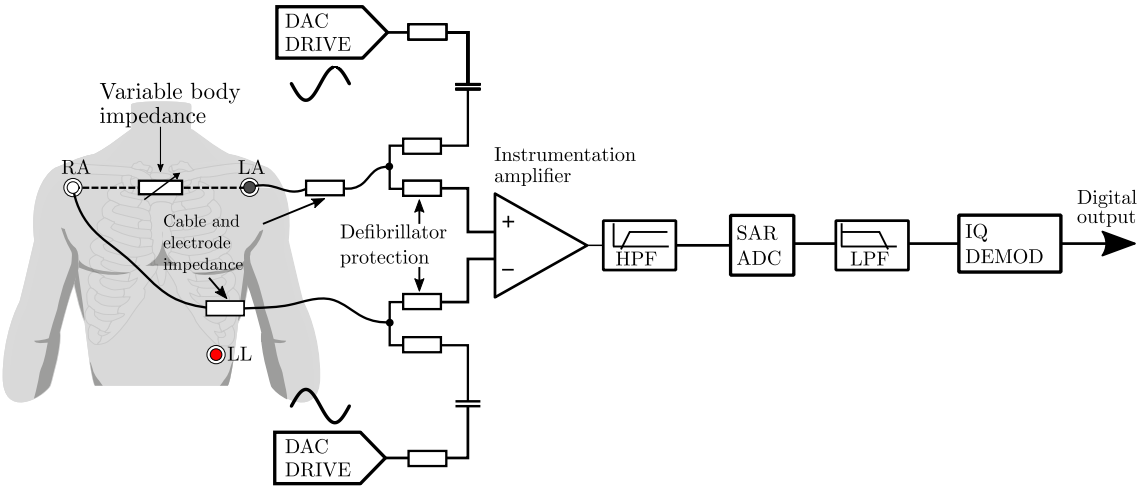

Figure 6: Block diagram for one lead bipolar IPG measurement circuit. Redrawn from (Redmond, 2013) by author.

The maximum allowed current that can be driven into the patient is dictated by IEC 60601-1 (2020, Table 3, p. 103). The limits are frequency-dependent for AC currents. The safe limits for patient auxiliary AC current for type CF applied part ranges from 10 μA below 1000 kHz to a maximum of 1 mA at 100 kHz. For type BF applied part safe limits range from 100 μA below 1000 kHz to 10 mA at AC. The types BF and CF determine the required safety level of the medical device/part. Type CF part provides the highest degree of patient protection whereas type BF part provides also high-level protection but is not suitable for direct cardiac applications such as esophageal ECG.

Typically, the drive frequency is set above 20 kHz to optimize the skin-to-electrode impedance. In lower frequencies, the skin-to-electrode impedance is relatively high and thus complicates the current injection. However, too high frequencies are not also desired, as stray capacitances can become problematic and the measurement becomes more vulnerable to interference. (Redmond, 2013)

2.2 Electrocardiogram (ECG)

One of the most central parameters for assessing the patients' blood circulation is an electrocardiogram. ECG measures the electrical activity of the heart from the surface of the body and plots the measured activity into a monitor screen or ECG paper. The sinoatrial node in the right atrium of the heart consists of pacemaker cells, which synchronously send electric signals propagating through the heart resulting in a complete cycle of cardiac contraction and relaxation, also known as heartbeat. These signals of around 100 mV action potential (Thaler, 2019, p. 25) can be measured propagating to the surface of the skin using medical electrodes. ECG is a powerful tool for clinicians and cardiologists and is used to detect cardiac abnormalities such as heart attack, cardiac arrest, or arrhythmia.

The electrical impulses from the heart are received using electrodes. The placement of the electrodes is crucial for successful measurement. Each electrode location provides a certain view of the heart's electrical activity. These views are called leads and planes, which are specified for each ECG variant. Leads view the electrical activity of the heart between two poles or points, a positive and negative. Planes give a cross-sectional perspective, namely horizontal and frontal representation of the electrical activity of the heart.

ECG electrodes (a.k.a. lead wires) are labeled and color-coded according to either American Heart Association (AHA) or International Electrotechnical Commission (IEC). In this work, we use the labeling and color-coding by AHA. The four basic electrode positions are at both arms and legs, denoted as right arm (RA), left arm (LA), right leg (RL), and left leg (LL). Electrodes, RA, LA, and LL form the standard three leads I, II, and III commonly known as the limb leads. These leads are placed either at the torso, surrounding the heart, or at the respectively notated limbs. These three leads form an imaginary triangle referred to as Einthoven's Triangle as seen in the Figure 7a. Leads I, II, and III are called bipolar leads, as they measure the voltage difference from one positive electrode to one negative electrode. The RL electrode has been traditionally used to ground the patient to the common ground, therefore not having a part in the formation of the leads. Additionally, in most modern applications, RL is used to drive the patient's body to the device's inner potential. This configuration is called right leg drive (RLD). RLD is supposed to bring the patient and measurement device to the same potential to reduce interference and noise in the measurement.

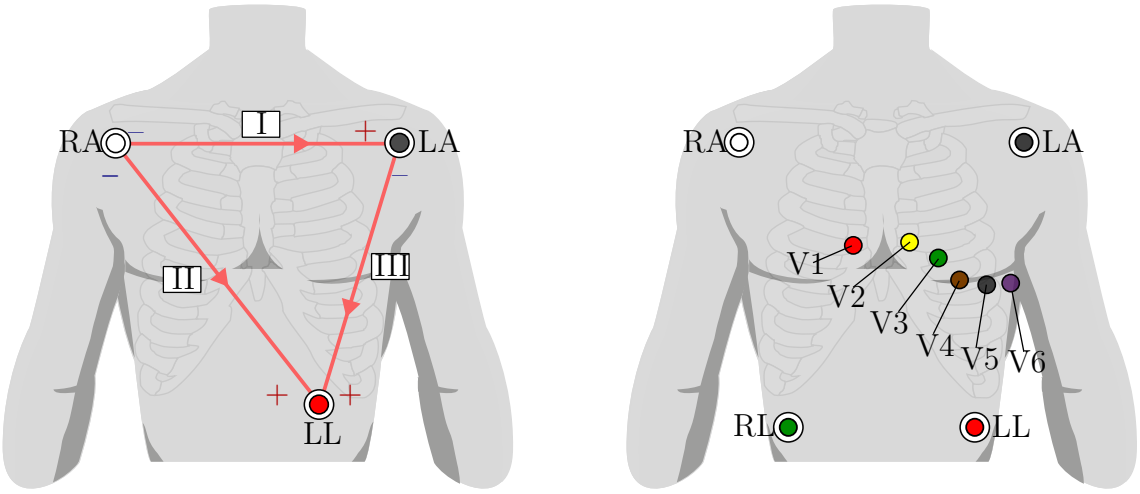

(a) 3-lead ECG with Einthoven's Triangle and three leads pictured.

(b) 12-lead ECG electrode placement with limb leads brought to the torso.

Figure 7: Two common ECG variations, 3-lead and 12-lead ECG.

At a minimum, ECG can be measured using only two electrodes, that is, one lead. However, to gain clinically satisfactory data, at least three leads are used to form a set of paired combinations, enabling differential measurements and vectors to represent the electrical activity from different directions.

Different variants of ECG are intended for varying uses in different environments. The most comprehensive and descriptive of the variations is the 12-lead ECG, as it provides the most angles of the heart for diagnosing. 12-lead ECG is the standard approach for diagnosing cardiac diseases such as coronary heart diseases and heart failure. However, a standard 12-lead ECG may not be feasible in every situation. Movement of the limbs can cause artifacts, which can interfere with the ECG reading. To reduce interference from the limb movement, limb electrodes can be placed on the torso as seen in the Figure 7b.

In patient monitoring, a reduced lead count ECG may be preferred in situations where there is no ongoing cardiac event, or the probability of an event is low. A 5- or 3-lead ECG can be used to obtain an adequate amount of information for monitoring purposes. Even one lead ECG can be sufficient for basic heart monitoring and checking for arrhythmias. ECG with fewer leads is quicker to set up and does not restrict the patient's movements as much as the 12-lead variant.

2.2.1 ECG waveform

The interpretation of ECG is done based on the sinus rhythm. The electrical activity originated from the cardiac muscle cells periodically oscillates during the cardiac cycle. The cardiac cycle is the time from the end of one heartbeat to the beginning of the next and consists of the diastolic and systolic phases. During the diastolic phase, the heart muscle relaxes, and the ventricles fill with blood. During systole, the heart muscle contracts rapidly, and the blood is pumped to circulation.

In an ECG measurement, the sinus rhythm appears as a series of waves, representing the sequence of depolarization and repolarization of the atria and ventricles. Figure 8 presents a standard scalar ECG waveform, also known as sinus rhythm. The specific pattern is recognized using wave annotations: P wave represents the activation of the left and right atrium, followed by the QRS complex representing the rapid ventricular depolarization. Finally, the T wave represents the repolarization of the ventricles followed by a tiny U wave, which represents the repolarization of the bundle of His. The U wave is almost indistinguishably small, hence being often omitted in ECG visualizations. (Martindale and D. F. M. Brown, 2017) The direction of the depolarization wave determines the polarity of the wave deflection. A positive deflection occurs when the repolarization wave spreads towards the positive pole of the lead. A negative deflection is seen when the depolarization wave spreads away from the positive pole towards the negative pole. Regardless of the lead count and used ECG variant, each lead represents a certain location of the heart's electrical activity. An anomaly present in a particular lead points to a location of the possible cardiac event. (A. L. Goldberger, Z. D. Goldberger, and Shvilkin, 2018)

Interpreting the ECG requires a trained eye and a clean signal. Aside from interpreting the clean signal, the operator needs to be aware of the different interferences and artifacts that can be present in the measurement. Artifacts can occur in ECG due to various causes, they can be patient, operator, environment, or device related as presented by Sörnmo and Laguna (2015). Patient-related interferences usually originate from patient movement or shiver, resulting in muscle artifacts or baseline wander caused by respiration or perspiration. Operator-related artifacts include ineffective skin preparation and lead placement. Environment-related interferences are generally caused by AC interference from fluorescent lights (Silva, Fernández-Chimeno, and Pallas-Areny, 1994) and related electromagnetic noise from the surrounding equipment. Equipment-related issues generally include defective electrodes, improper grounding, or equipment malfunctions.

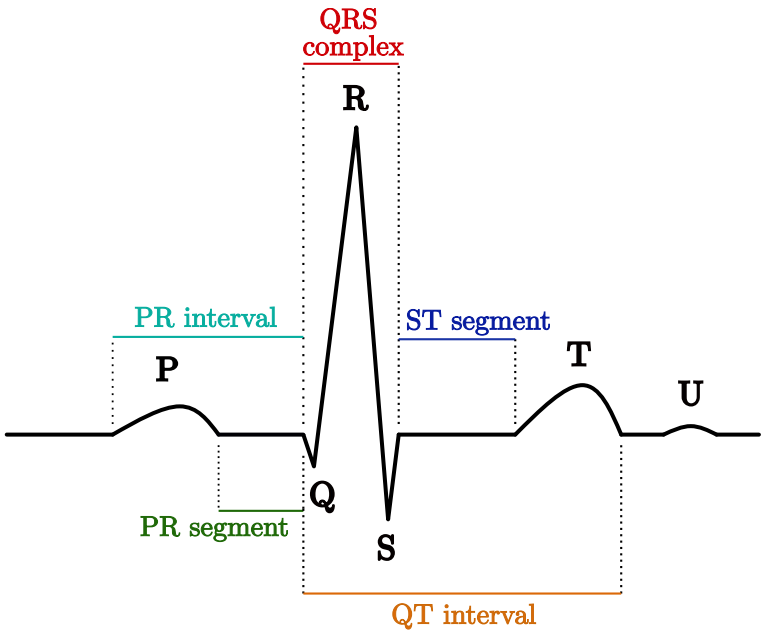

Figure 8: A standard representation of an ECG waveform and sinus rhythm with PQRST sequence.

2.2.2 Measuring ECG with biopotential amplifiers

As introduced in the previous subsections, ECG is a highly sensitive biopotential measurement between two points on the surface of the patient's body. The signals originating from the heart get attenuated while traveling to the surface of the skin, resulting in a signal of few millivolts or less in amplitude (Webster and Nimunkar, 2020, p. 8). Measuring this kind of faint signal requires a specially designed amplifier circuit.

Amplifiers are used to increase signal strength while simultaneously maintaining high precision and accuracy. Biopotential amplifiers are specifically fitted to measure biosignals, including ECG. A biopotential amplifier must have high input impedance to prevent loading and thus distorting the measured signal. In practice, modern complementary metal-oxide-semiconductor (CMOS) amplifiers have input impedances generally in the range of tens of giga ohms. On the contrary, the output impedance of the amplifier needs to be low to allow driving of any load such as indicating or recording device without sacrificing fidelity or range.

In order to obtain an optimal signal-to-noise ratio (SNR), it is important to limit the amplifier bandwidth to just barely fit the frequency spectrum of the biosignals. The frequency spectrum of an ECG signal is 0.01–250 Hz depending on required precision (Tagawa, Tamura, and Oberg, 2011, p. 283). Often, the clinically significant information can be found in the spectral band 0–100 Hz (Gupta, Mitra, and Bera, 2013, p. 52), which would locate the needed sampling rate to around 200–500 samples per second. Nyquist rate (a.k.a. Shannon–Nyquist criterion) claims that a band-limited signal can be perfectly reconstructed provided that the sampling frequency exceeds twice the bandwidth (BW) of the signal, that is, 200 Hz in this case (Pamula,

Hoof, and Verhelst, 2019, p. 33). In practice, the sampling rate is often set some multiples higher to factor in the step response of the filters.

For bipolar electrode configuration, such as leads I, II, and III in ECG, electrodes are electrically symmetrically located with respect to ground. Therefore, a differential amplifier is the most appropriate choice. Differential amplifier outputs and amplifies only the voltage difference between the two input pins. Bipolar electrodes often suffer from electrode DC offset voltage, which must be taken into account when determining the DC range of the amplifier. Offset voltages up to 300 mV can be sensed between the electrodes, on top of which the amplifier has to be able to measure the actual ECG signal.

Figure 9 shows a traditional analog front-end circuit for 4-electrode ECG measurement with RLD. The leads are multiplexed to an instrumentation amplifier differentially and the buffered output is used to drive the patient body to the Wilson center terminal potential.

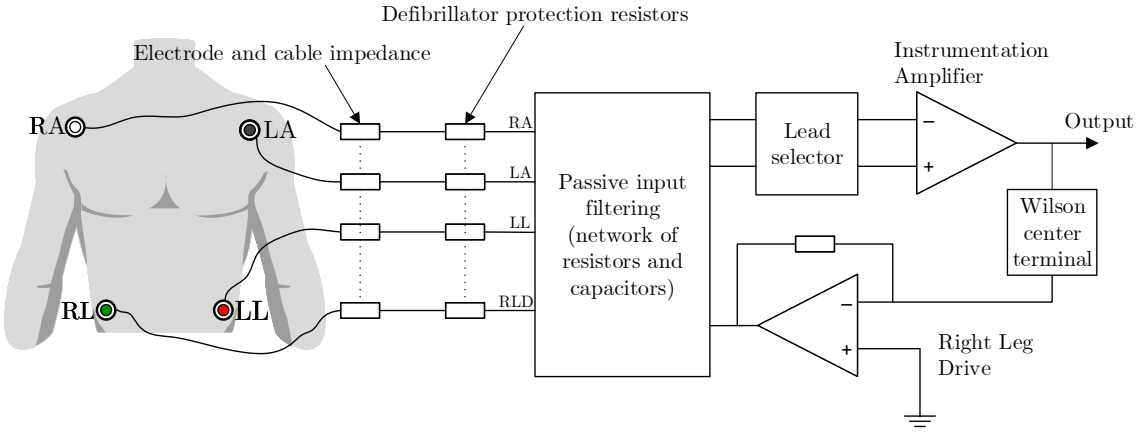

Figure 9: A traditional analog front-end circuit for 4-electrode ECG measurement with RLD.

2.3 Electromagnetic interference in bio-electrical measurements

Measuring the faint biosignals introduced in the previous sections is not a substantial challenge for modern amplifiers and analog front ends. The real complexity of the measurement originates from the variables created by the real-life surroundings and environment. The world is full of electromagnetic interference originating from different natural and man-made sources, which can affect the operation of an electronic device. Natural sources such as rain and thunderstorms originate from the earth's atmosphere. Extra-terrestrial sources originate from outer space, such as solar radiation and cosmic noise. The man-made sources include all kinds of electronic devices such as electric motors, power lines, computers, radios, power tools, and mobile networks, to name a few (Kaiser, 2004). According to GSMA (2020), there are over 5 billion unique mobile network subscribers in the world. The rapid development of wirelessly transmitting smartphones, IoT devices, and networking devices in the last decades could not have been possible without careful consideration of the electromagnetic interference present in the modern world.

2.3.1 Interference and noise

The terms *interference* and *noise* are easily misinterpreted and mixed with each other. Ott, 2009, p. 3 describes the noise as "any electrical signal present in a circuit other than the desired signal" and interference as "the undesirable effect of noise." For example, when having a conversation with a friend at a restaurant, the other people talking is noise. When the conversation is negatively affected by the noise, it becomes interference.

Each electronic system will have at least some amount of noise present, whether it originates from the circuit itself or from outside sources. It is only when the noise causes undesired operation of the circuit, it becomes interference. Often, the noise cannot be eliminated, and it is the job of the engineer to prevent it from becoming interference. Alternatively, the magnitude of the noise can be reduced, until it no longer causes interference.

In bioelectronics engineering, often the most commonly problematic noise is the power-line noise. Power-line noise (a.k.a. mains noise, AC noise) originates from electronic devices and transmission lines present in our surroundings. This sinusoidal 50 or 60 Hz electromagnetic interference can often be heard coupling into audio equipment such as speakers, making an audible low-frequency humming sound. This same noise can travel over air coupling to biomedical measurements, such as IPG or ECG, causing common-mode interference to the measurement input (Webster and Nimunkar, 2020, p. 352). The main reason why power line interference is problematic is in its frequency. The 50 or 60 Hz interference sits directly in the frequency band of the ECG signal where it cannot be filtered easily.

2.3.2 Common mode interference

Probably the most prevalent form of electromagnetic interference in RR and ECG monitoring is common-mode voltage. Common-mode voltage often originates from the electric power-line noise surrounding the measurement environment, which the human body is highly efficient in picking up. Webster and Nimunkar, 2020, p. 352 describes the phenomenon as if the entities are connected to the power lines through small capacitors. This model is further visualized for wearable ECG devices in the Figure 10. As a result, the patient's body potential fluctuates within tens of volts in magnitude, conducting through the electrodes and cabling to the measurement front end. Power-line noise can also couple directly to the electrode cables. In RR and ECG measurements, the signals are measured between two electrodes at a time with a differential amplifier. Therefore, the power-line interference is coupled into both ends of the differential measurement, hence the voltage being common to one another.

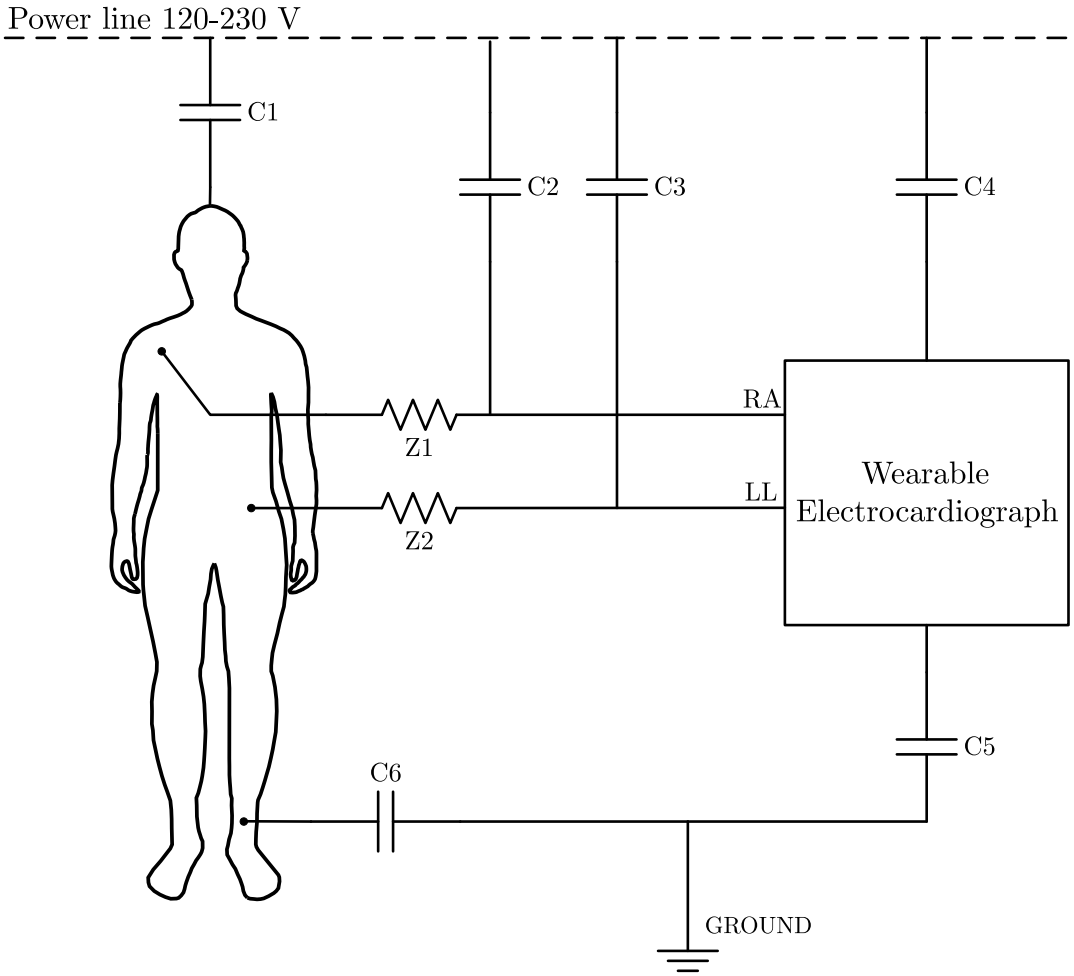

Figure 10: Power line noise couples to the patient, wearable ECG device and electrode cables through a small capacitance. Similarly, the patient and the ECG device is capacitively coupled to the ground. Figure redrawn from Webster and Nimunkar (2020, p. 353).

An ideal differential amplifier responds only to the difference in the voltages applied to its input terminals. Even though today's amplifiers are highly efficient, some amount of common-mode voltage still may leak through to the amplifier's output. One reason for this is the slightly different gain between the amplifier input terminals, known as common mode response. The common-mode response of each amplifier is often disclosed in the product datasheet. The primary reason for the common-mode voltage at the amplifier output originates from the passive components at the amplifier inputs. The input of a biopotential amplifier often consists of various passive components designed to filter and control the currents through the patient. Additionally, the variation in the contact impedance of the measurement electrodes introduces another variable to the total impedance of the amplifier's input terminal. Therefore, a pure common-mode signal in the amplifier inputs is not viewed as a significant issue. The underlying challenge is to prevent the transformation of the common-mode signal to a differential signal. This can happen due to the differences in electrode-skin contact impedances and cable capacitance, as well as because of defibrillation protection and filtration circuits in the analog front-end. Therefore, the CMRR abilities of the amplifier are insignificant compared to the proper design and impedance matching of the input circuitry.

The ratio of differentially applied signal and common mode response is called the common-mode rejection ratio (CMRR). It can also be expressed in decibels by taking 20 times the logarithm of CMRR value (Clayton and Winder, 2003). The decibel presentation is often denoted as CMR. The higher the CMRR or CMR value is, the better the amplifier is at rejecting the common-mode voltage.

2.3.3 Radiofrequency interference

Another prevalent source of interference is wireless communications equipment such as mobile phones, wireless transmitters, radios, and broadcasting towers. These types of devices emit electromagnetic waves at radio frequencies (RF), which in the early days have been shown to negatively affect the performance of electronic medical devices leading to even banning the use of personal mobile phones in some hospitals (Bit-Babik et al., 2007). The frequency bands and modulations commonly emitted from wireless communications equipment have been since addressed in the standard requirements electromagnetic immunity of medical devices.

The equipment transmitting signals at the radio frequency spectrum generates an electromagnetic field to the surrounding environment. The electromagnetic field causes currents and voltages in the devices depending on the resonant frequency of the device's physical dimensions. Some medical devices are more sensitive to electromagnetic coupling than others, leading to establishing comprehensive standard requirements for electromagnetic compatibility in different types and categories of medical devices.

With ECG and RR sensors, the parts that are often the most susceptible to electromagnetic interference are the electrode lead wires. Since a wireless patient monitor can be very small in size, the lower frequency waves do not likely pose problems to the device itself. However, the length, orientation, and overall area

encompassed by the electrode lead wires present a real challenge that cannot be solved by only designing a small and wearable device. Since the lead wires have to reach different parts of the body, their length is physically limited and cannot be altered beyond a certain extend. The lead wires can form several kinds of bundles and inductive loops that are especially vulnerable to electromagnetic waves. The bundle of lead wires basically forms a type of antenna with a certain resonant frequency depending on the area and layout of the bundle. Within its resonant frequency, the "antenna" has the lowest impedance and thus the electric field coupling is at strongest. Typically, antenna resonant frequency can be found by looking at the size of the radiation element. The resonant frequency can be calculated with the formula

$$\text{Freq} = \frac{c}{\lambda},$$

where c is the light speed, namely 299,792,458 meters per second, and λ is the receiver wavelength determined by the type and size of the antenna. Therefore, for example, a simple quarter-wavelength dipole antenna with a radiation element length of 10 cm would have a resonant frequency of 750 MHz.

It is possible to use shielded lead wires to try to minimize the coupling of the interference, but in some applications, they might not be feasible due to the added cost and wire gauge. It is important to consider the interference in the lead wires already during the design of the analog front end of a bioelectrical sensor. Engineering tests to ensure EMC compliance is often conducted already at the design phases to catch any potential underlying issues early on. Eventually, the device has to be tested in an official standard test setup, where it becomes very expensive to fail.

2.3.4 Standard requirements for electromagnetic immunity

Various government entities set regulations according to standards developed by international committees for the electromagnetic functionalities of electronic devices in the market. These entities include Federal Communications Commission (FCC), International Electrotechnical Commission (IEC), and International Special Committee on Radio Interference (CISPR) to name a few. The regulations are enforced by governments by requiring electromagnetic compatibility and immunity testing of the products going to the market. Electromagnetic compatibility translates to the ability of an electronic device to work reliably in its environment. In practice, this means that the emissions from the device are controlled and predictable. It also considers the immunity of the device to interference coming from outside the system. Simply, the electronic device should not be able to cause other devices to malfunction due to excessive radiation, and withstand reasonable amounts of radiation itself without malfunctioning. These rules apply to all electronic devices regardless of the field and application. However, there are additional standards for medical equipment to underline the specific performance requirements for medical devices used in the hospital environment. A medical device cannot be released into the market before compliance with the requirements is proven by standard testing.

IEC 60601 is a series of technical standards for the safety and essential performance of medical electrical equipment. It consists of the general standard, about 10 collateral

standards, and about 80 particular standards. The general standard IEC 60601-1 defines the general requirements for basic safety and essential performance for medical devices. In addition, collateral standard IEC 60601-1-2 (2020) further addresses the requirements and tests for electromagnetic disturbances in medical electrical equipment. IEC 61000-4-3 (2020) and IEC 61000-4-6 (2013) define the required EMC test methods for radiated radio frequency electromagnetic field immunity tests. Particular standards such as IEC 80601-2-49 (2018) and IEC 60601-1-2-27 (2011) amend and supplement the general standard with requirements for multi-functional patient monitoring and ECG monitoring devices. The precise standard defined test levels and methods applied in this work are discussed further in the next chapter.

3 Materials and methods

This chapter describes the research methodology and materials used in this thesis. First, a design description and properties of the designed dual-parameter sensor prototype are presented. Next, a deeper dive is taken into the core functionalities of the ADPD4100 analog front end, also describing the sensor front end measurement model for ECG and IPG based RR (hereafter just RR). Finally, test methods for the EMC feasibility analysis of the developed dual-parameter sensor front-end are presented in detail.

3.1 The multimodal dual-parameter sensor prototype

The work that serves as a background for this research consists of a preliminary evaluation of the ADPD4100 analog front-end chipset produced by Analog Devices, Inc. (ADI). The feasibility of the chipset has been tested at GE Healthcare for both ECG and RR measurement using a prefabricated commercial evaluation board "EVAL-ADPD4100". To simulate a typical environment for wireless and wearable patient monitor, the evaluation board was battery operated and the measurement data was transferred wirelessly to a receiver. The preliminary results showed that the ADPD4100 is feasible for obtaining one lead ECG and two channels of RR with time multiplexing, providing an initial proof of concept. Additionally, the feasibility of the AFE was studied in an EMC test setup, which demonstrated promising results for the electromagnetic immunity of the analog front-end.

However, the evaluation board used in the feasibility study was originally designed for wrist-based photoplethysmography and thus was not especially optimized for ECG and RR measurement. Furthermore, the evaluation board consisted of two separate circuit boards conjoined with ribbon cable. This setup was not representative of a compact wireless sensor and thus the EMC performance could not be indisputably assessed. To gain a deeper understanding of the true potential of the chipset for ECG and RR measurements, the passive front-end circuit would need to be redesigned. IEC 80601-2-49, 2018, p. 13 states that parts associated with multifunction patient monitors are classified as *defibrillation-proof applied parts* providing the highest degree of patient protection. According to IEC 60601-1, 2020, p. 91, any defibrillator-proof applied part needs to be protected against the effects of a discharge of a cardiac defibrillator to the patient. This is often done by utilizing high voltage pulse withstanding resistors to the input of the patient connected cables and instruments (Becchetti and Neri, 2013, p. 170). Additionally, the filter components at the front end should be optimized for better EMI rejection and tolerance.

In order to evaluate the novel measurement principle in a real setting, a proprietary prototype of the sensing front end with required wireless functionalities was developed. The design requirements for the prototype for feasibility analysis were identified based on the findings from the earlier benchmarks. The electronics design of the prototype was carried out by the author, while the measurement acquisition software was developed by Kim Blomqvist. The simulations and innovations to the passive circuit of the AFE have been done in a group effort by engineers of GE Healthcare

Finland and Analog Devices, Inc.

The developed prototype (pictured in Figure 11) includes wireless communications functionality with Bluetooth Low Energy (BLE) and is battery powered. Wireless and portable operation allow the feasibility analysis to occur in a natural use-case environment, operating as a wireless and wearable patient monitoring sensor without external cabling for data communication or power delivery. The front-end of the prototype includes the ADPD4100 and a specifically designed passive front-end circuit. At the input, there are three-electrode connectors correspondingly notated as RA, LA, and LL. In essence, the prototype works as a standalone sensor that can be connected to any compatible BLE receiver such as PC, smartphone, or a BLE radio development board. The key features of the designed sensor prototype are presented in the list below.

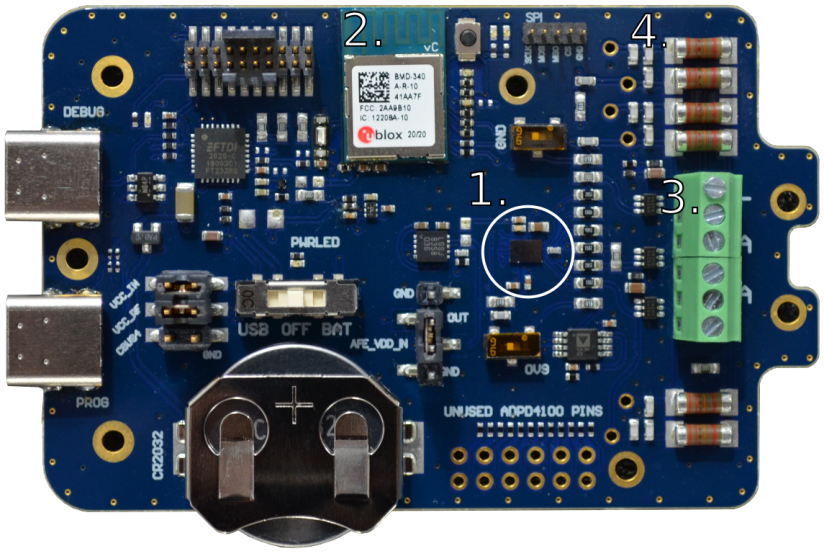

Figure 11: The dual-parameter sensor prototype. The most essential parts of the design are numbered as follows: 1. ADPD4100 multimodal analog front end 2. ublox BMD-340 BLE MCU module 3. electrode lead wire connector terminal 4. defibrillation protection resistors.

- Bluetooth low energy (BLE) and IEEE 802.15.4 wireless communication,
- Arm® Cortex®-M4 with floating point unit (FPU) 32-bit processor,
- ADPD4100 multimodal sensor front-end IC,
- Serial Peripheral Interface (SPI) communication,

- 3V DC via single use coin cell battery (CR2032),
- optional 5V DC via USB-C connector,
- FTDI RS323 converter to USB,
- AFE input filtering circuit with several possibilities for re-configurations, and
- three terminal electrode connector for RA, LA and LL

A high-level block diagram of the design is presented in the Figure 12. A single-use coin cell battery (CR2032) works as a main power source for the sensor. Alternatively, the sensor can be powered through a USB-C connector. The input voltage is monitored by a voltage supervisor circuit which drives the *ENABLE* pins of two 1.8 V linear voltage regulators. If the voltage of the battery or the USB-C supply decreases too much, the power is automatically cut from the system by the supervisor. The two regulators supply power to the rest of the circuit. The BMD-340 BLE radio module is responsible for the wireless and wired data communication to the receiver, receiving the measurement data from the AFE through SPI, and driving any other peripherals such as the user interface's light-emitting diodes (LED). The BMD-340 can be programmed through the Joint Test Action Group (JTAG) port fitted in the sensor printed circuit board assembly. Additionally, the ADPD4100 configuration parameters are sent through the SPI by the BMD-340. The ADPD4100 performs the ECG and RR measurements acquiring the signals which are stored in a first in first out (FIFO) register from where it is periodically read by the BLE radio module via SPI. Serial line internet protocol (SLIP) was used in the data transmission and an 8-bit check number (XOR) and frame counter were added to each data frame. This way it could be ensured, that the received data was whole, and no frames were lost during the transmission.

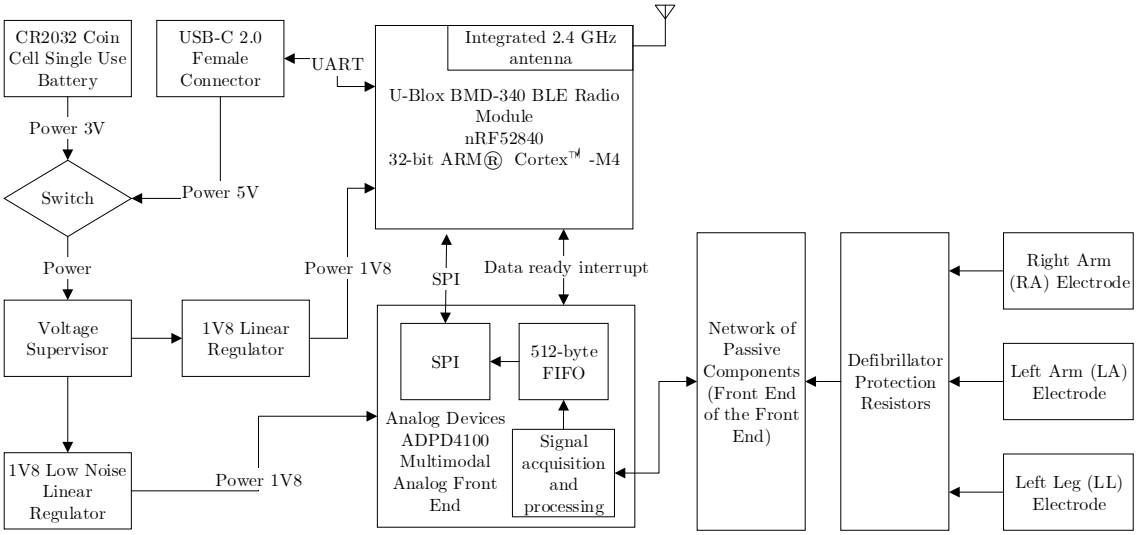

Figure 12: Block diagram of the designed dual-parameter sensor prototype

The ability of the prototype to accurately acquire ECG and RR signals was evaluated by both using a patient simulator (Figure 13) and with a volunteer human subject (Figure 14). The simulator used in the test was a Fluke ProSim8 vital signs simulator. The simulator was configured to output RR signal at an amplitude of 5 Ω and one lead ECG with amplitude of 1 mV. The simulator did not support outputting dual RR signals simultaneously, so for RA - LA and RA - LL leads, the RR signals were activated subsequently.

For the test with a human subject, a proprietary electrode patch assembly was attached to the chest of the subject in their respective locations as previously described in the 3-lead ECG setup in Figure 7a. The subject was instructed to sit in an office chair in a slightly reclined position. The electrode patch assembly was connected to the EUT and the measurement was started. The subject was instructed to breathe normally.

Approximately 30 seconds of data were recorded in both test cases. The data was then filtered forward-backward with 1st order 40 Hz Butterworth lowpass filter for ECG and 1st order 20 Hz Butterworth lowpass filter for RR channels to get rid of the majority of unwanted noise in the signal.

In addition to testing the biosignal acquisition, the internal noise level of the prototype was measured. The peak-to-peak noise for RR was measured at 70-150 mΩ. Respiration-caused impedance changes can be even as small as 100 mΩ, which can get buried into the noise. The noise level of ECG was better, but interesting peaks at multiples of 30 Hz were found in the spectrum analysis of data. The origin of the peaks was not found during this work.

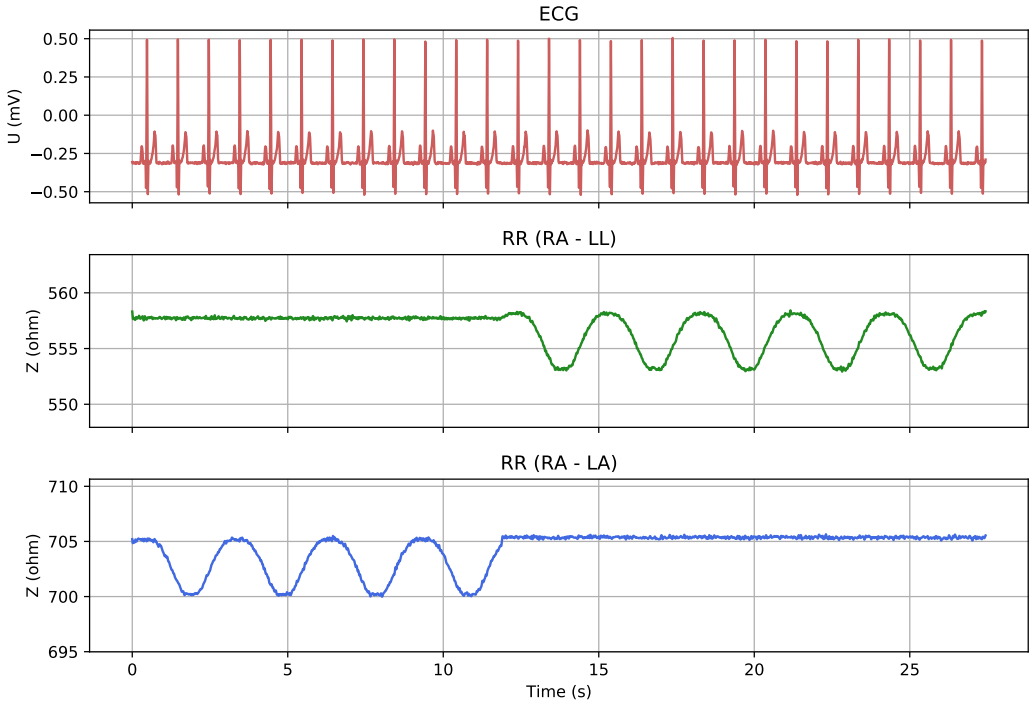

Figure 13: Biosignal measurement with the dual-parameter sensor prototype using Fluke ProSim8 patient simulator.

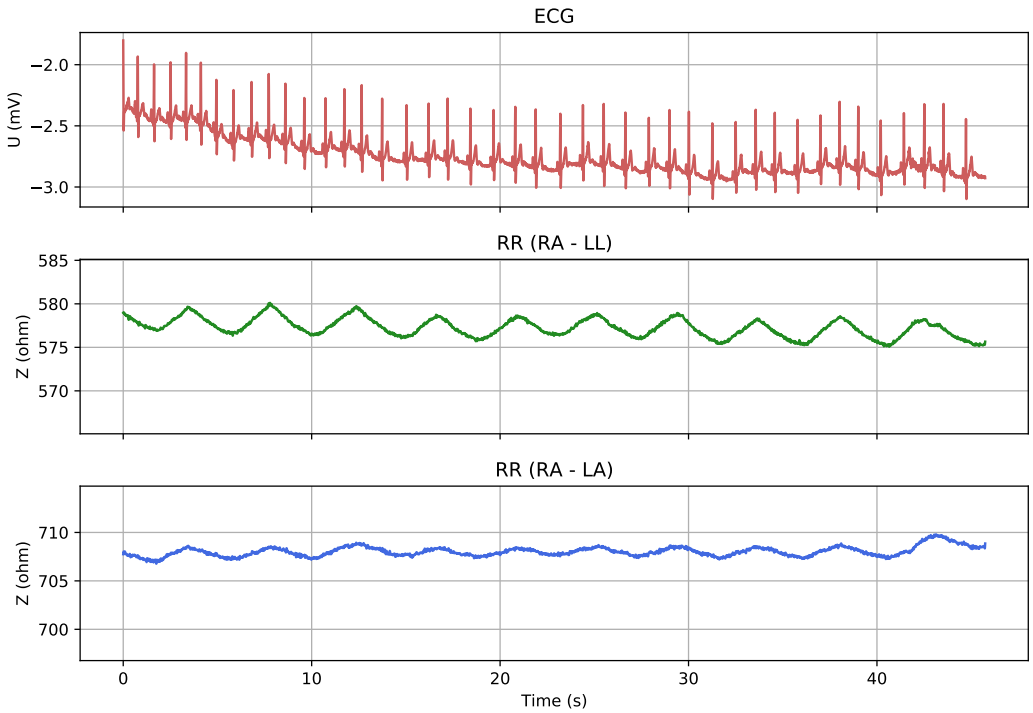

Figure 14: Biosignal measurement with the dual-parameter sensor prototype with electrodes attached to a human subject.

3.1.1 Analog Devices ADPD4100

The chipset selected for this work is the Analog Devices ADPD4100 multimodal sensor front end. ADPD4100 is originally designed for optical sensing applications such as photoplethysmography and optical heart rate measurement. It drives up to eight LED's and measures the return signal on up to eight single-ended or four differential current inputs. However, the provided multiple operation modes within the chipset enable the ADPD4100 to be used for various sensor measurements. The sensor front end provides 12 time slots enabling up to 12 separate measurements per sampling period, making it suitable for time-division multiplexing of ECG and RR. A block diagram of the ADPD4100 is presented in Figure **??**. ADPD4100 consists of a TIA inputs, signal conditioning, integrator, and analog-to-digital converter (ADC). The LED drivers function as current sinks of which four can be driven simultaneously. The digital block provides multiple operating modes, programmable timing and four general-purpose input/output (GPIO) pins enabling various sensor measurement configurations.

The AFE signal path consists of eight TIA current inputs which can be driven either in differential pairs or single-ended configurations. Each channel is equipped with TIA with programmable gain, a band-pass filter, and an integrator. Finally, the channels are time-multiplexed into a 14-bit ADC. The complete input sampling circuit is presented in the Figure 15. Resistors notated R_F are the TIA feedback resistors and R_{INT} represents the series resistors the input of the integrator.

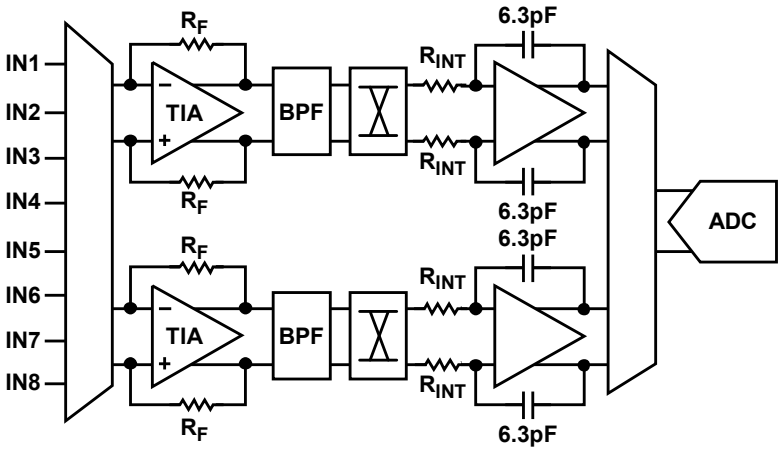

Figure 15: ADPD4100 input multiplexing circuit. (Analog Devices, Inc., 2020, with permission)

Figure 16 shows a more detailed view of the complex switch matrix at the analog input pairs. The programmable switch matrix enables the connection to the two AFE channels.

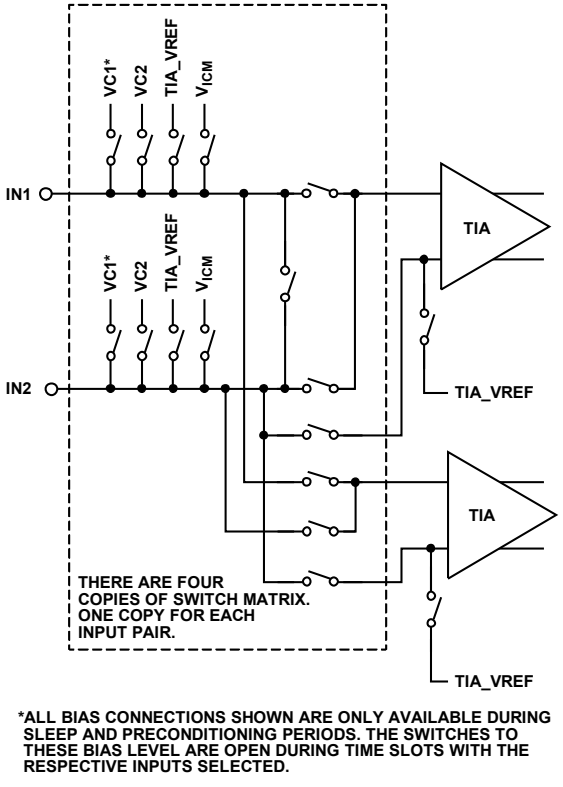

Figure 16: The complex multiplexer switch network at each analog input pair. (Analog Devices, Inc., 2020, with permission)

3.1.2 Design of the analog sensor front-end

This section covers a more detailed description of the operation and design of the analog front end for the dual-parameter prototype. The AFE of the sensor acts as a time-multiplexed sampling circuit for measuring one lead ECG and dual vector RR waveforms. In addition to the ADPD4100 chip, the time-multiplexed measurement principle requires a specifically engineered passive input filtering circuit, that is, the "front end of the front end" shown in Figure 17. The purpose of this circuit is to allow the coexistence of the three measurements within the same measurement leads.

Within the front-end, the RR is measured across the transthoracic and transdiaphragmatic planes (approximately as standard lead I between LA and RA and lead II between LL and RA) where the RA electrode acts as an electrical reference. The measurement current is supplied successively to the LA and LL electrodes, while simultaneously measuring the corresponding voltage between the electrodes with the transimpedance amplifier (TIA).

All patient coupled connections are isolated with defibrillator pulse withstanding 22 kΩ resistors. These resistors are the first point of contact from the lead wires, where they act as first buffers to any unwanted external voltages such as from a defibrillator pulse. The resistance of the protection resistors should be kept as minimal as possible to minimize attenuation of IPG drive currents and maximizing SNR, while still offering a needed level of protection to the patient and the device.

The rest of the circuit consists of EMC filtering capacitors and additional defibrillator protection resistors near the TIA input pins. In the current drives, there are also additional DC block capacitors to remove the DC components from the injection current.

Next, the measurement methodology is presented in detail concentrating on one of the three sequential time slots at a time.

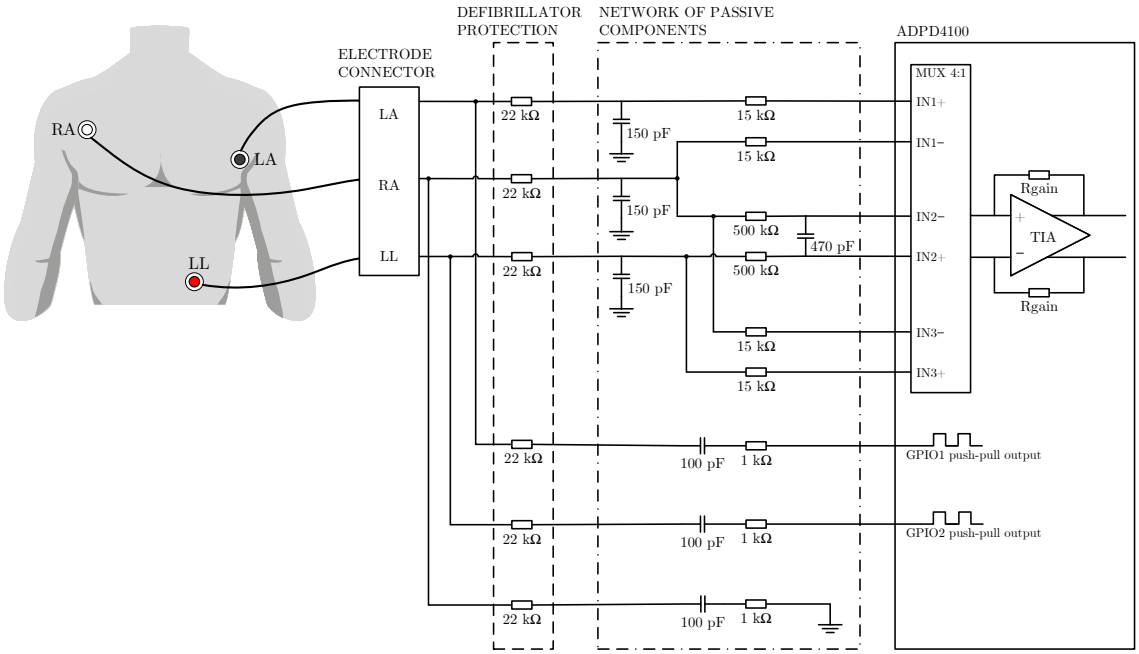

Figure 17: The analog front-end circuit of the dual-parameter sensor prototype

The measurement begins with a sampling of the ECG (Figure 18) by connecting the TIA input IN2 few times briefly to the 470 pF sensing capacitor. The capacitor discharges during the TIA connection and charges again when disconnected. The other channels are silent during ECG acquisition and there is a short sleep period to allow DC to settle after consecutive series of current pulses. This connection differs from a traditional ECG measurement circuit by introducing the sampling capacitor in the input of the TIA together with the time-multiplexed acquisition. The samples are stored into ADPD4100 FIFO register while the next measurement slot activates.

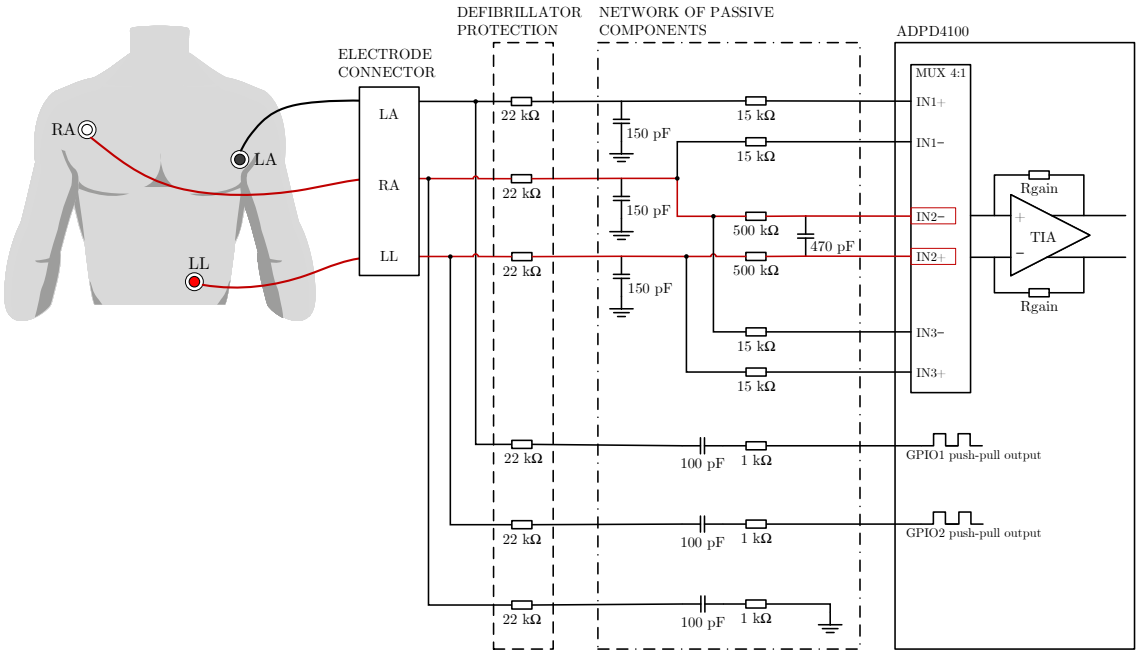

Figure 18: The sensing path for ECG measurement (time slot A) highlighted in red.

RR is measured with the bipolar method, implying that the current injection and the voltage detection are done in separate circuits. However, this should not be mixed with the tetrapolar measurement with separate electrodes for current injection and voltage sensing (see Section 2.1.1). These circuits only join after individual defibrillation protection resistors at each wire, effectively reducing the effect of the lead resistances.

The two RR vectors are measured in sequential time slots. Therefore, two separate current drives and voltage sensing channels are needed. The ADPD4100 includes four GPIO pins with a push-pull output configuration. Two GPIO pins are connected to electrodes (LA and LL respectively) through a DC block and defibrillator protection. The current injection is generated by sequentially pulsating the GPIO between high and low states, generating alternating current flowing to the body. The voltage produced by the current and body impedance is then measured with the TIA with the help of the passive components at the AFE input. Of the remaining two GPIO pins, one is utilized to send an interrupt to the MCU when the FIFO reaches the data limit. The remaining GPIO was routed as an option to drive an opposite phase pulse to the sense ground path to increase the overall potential in the injection current path.

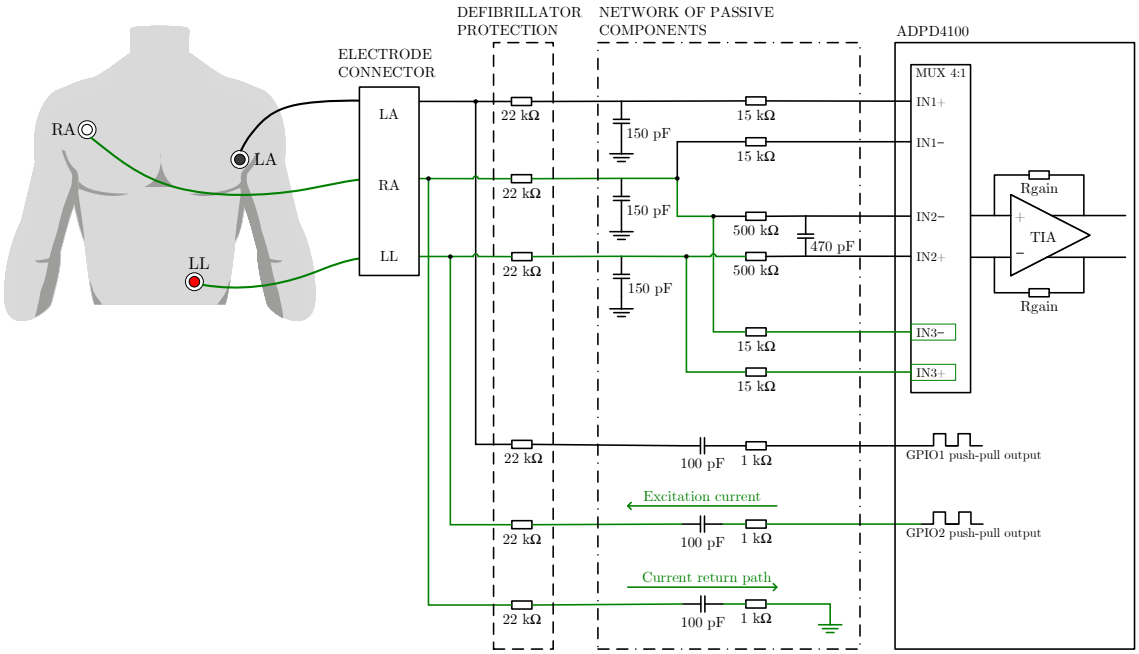

Figure 19: The sensing path of RR lead LL – RA (time slot B) measurement highlighted in green.

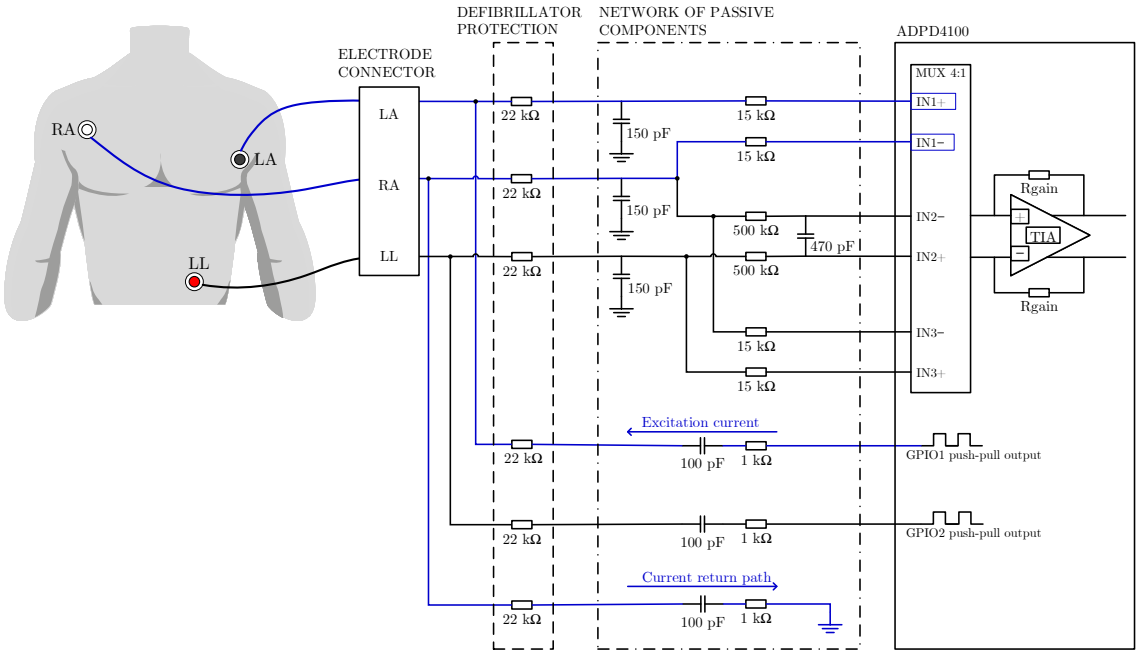

Figure 20: The sensing path of RR lead LA – RA (time slot C) measurement highlighted in green.

A simplified flow chart of the measurement principle is shown in the Figure 21. The application waits until the sensor is connected to a compatible receiver unit. After a successful connection, the ADPD4100 is configured through SPI to start

the measurement function. The measurement software works by sampling the three channels at a rate of 300 samples per second. ECG is measured first to avoid the RR measurement from affecting the baseline. Next, the two vectors of RR are measured sequentially. This loop is repeated until the amount of data reaches the set limit for the FIFO register. Then, the AFE sends a "data ready" interrupt to the BLE MCU which then reads the contents of the FIFO, processes it, and sends it over the air to the receiver unit.

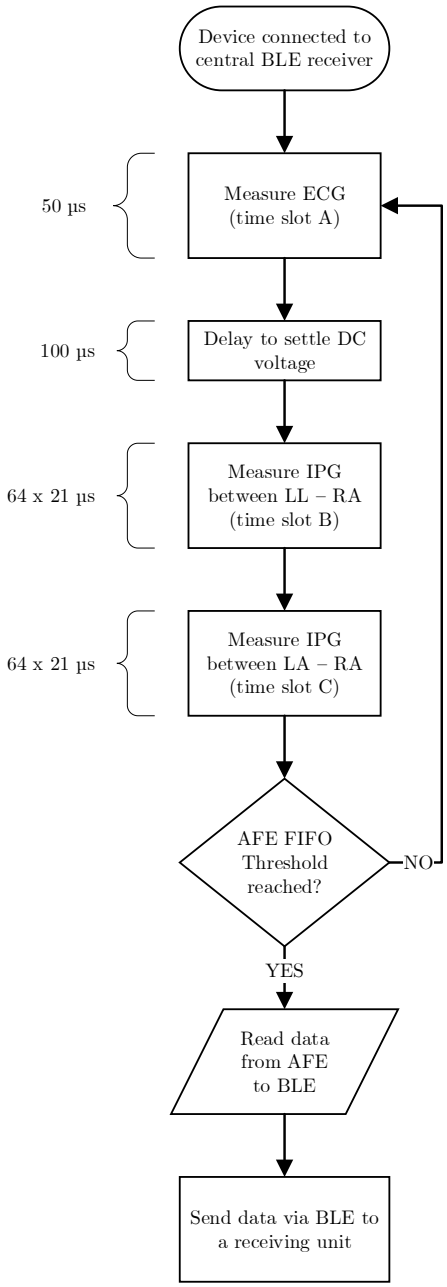

Figure 21: Simplified sensor software flow chart with timing information for each measurement slot.

3.2 Electromagnetic immunity compliance tests

The standard compliance test for the electromagnetic immunity of the novel design was performed in specifically designed test chambers at GE Healthcare Finland premises in Helsinki. The international collateral standard IEC 60601-1-2 defines the required frequency bands, immunity test levels, and modulation characteristics for the EMC testing of medical devices. Complementing standards IEC 61000-4-3 and IEC 61000-4-6 define the required test levels and testing and measurement procedures. Of these requirements and methods, the three most critical test cases were selected for this work which are described in Table 1.

Table 1: Standard defined EMC phenomena selected for the tests in this work.

Phenomenon	**EMC standard**	**Immunity test levels**	**Modulation**
Radiated RF EM Fields	IEC61000-4-3	3 V/m 80 MHz – 2.7 GHz	80 % AM at 2 Hz
Proximity fields from RF wireless communications equipment	IEC61000-4-3	28 V/m 385 MHz – 2.7 GHz	Pulse modulation at 18 Hz 50 % duty cycle
Conducted disturbances induced by RF fields	IEC 61000-4-6	3 V (before modulation) 25 MHz – 80 MHz 6 V (before modulation) in ISM bands between 25 MHz and 80 MHz	80 % AM at 2 Hz

Briefly summarized, radiated RF EM fields test the ability of the EUT to operate as intended when exposed to amplitude modulated signal to the enclosure, power, and signal ports of the EUT. Proximity fields from RF wireless communications equipment are tested in a similar fashion, but with higher electric field strength (28 V/m) and with pulse modulation instead of amplitude modulation, and also a narrower frequency band consisting of typical frequencies used in cellphones and other devices utilizing radio communication. Conducted disturbances continue the radiated RF EM field tests in a lower frequency range, which often cannot be tested in typical anechoic chamber due to the wavelengths surpassing the chamber dimensions.

3.2.1 Radiated RF electromagnetic fields

Test equipment and setup

IEC 61000-4-3 recommends testing to take place in an anechoic chamber of adequate size to maintain a uniform field with respect to the size of EUT. Additionally, recommended test equipment includes an RF signal generator, power amplifier, optional absorbers to damp reflections, field generating antenna, isotropic field sensor, and power measurement device for the forward power to name a few. The anechoic chamber at GE Healthcare Finland Helsinki fulfills these standard requirements and recommendations down to 80 MHz and therefore is suitable for performing EMC engineering tests. Figure 22 gives an overview of the complete test setup used in the testing. Testing at frequencies above 1 GHz requires a slightly modified setup

since the frequency range for the used broadband antenna is up to 1 GHz. This forces conducting the >1 GHz wideband part of the test in a separate test run with different horn-type field generating antenna.

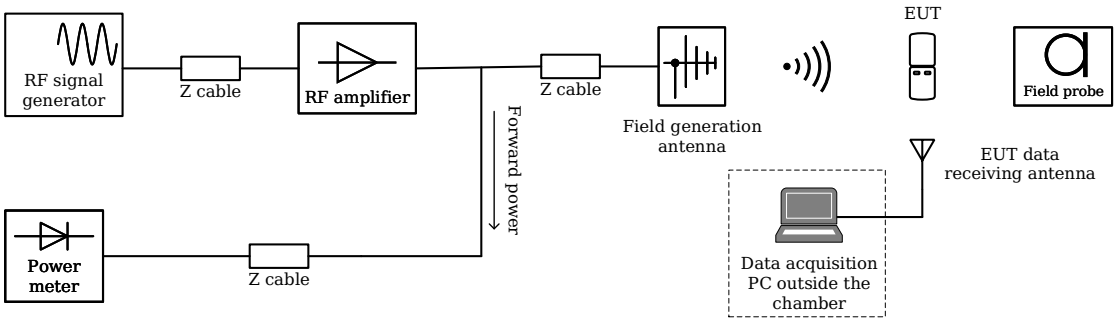

Figure 22: Test setup for the radiated RF electromagnetic fields immunity tests.

The IEC60601-1-2-27 standard for the safety and essential performance of electrocardiographic monitoring equipment defines the requirements for the positioning of the ECG lead wires during the radiated immunity testing. The standard recommends arranging the lead wires on the test table in loops with a gap of 5 cm between the wires. The overall width of the lead wire setup should be 30 cm. Figure 23 presents the applied looping in a nonconductive acrylic sheet with lead wires connected to the EUT.

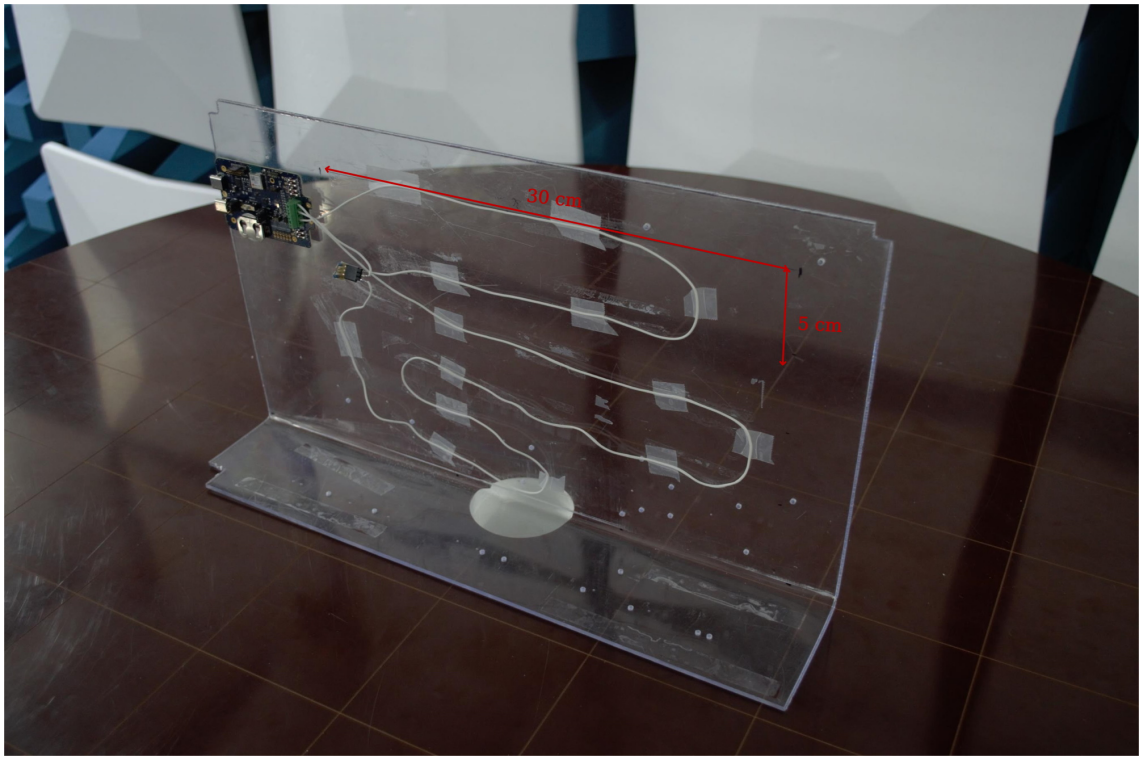

Figure 23: Electrode lead wire test sheet with standard specified looping of the cable and patient simulating electrode model.

At the end of each lead wire, there was a patient simulating load consisting of a parallel-connected resistor and capacitor. The purpose of the load is to simulate the impedance of a patient with medical electrodes applied to the skin. IEC60601-1-2-27 defines the load for 40 Hz ECG measurement as a 51 kΩ resistor and a 47 nF capacitor for each electrode. As we had both ECG and RR measurements with high frequency (approx. 50 kHz) current injection, the capacitor values were modified such, that the used capacitor size was 6.8 nF instead of 47 nF. The ECG still senses the resistive component of 51 kΩ resistor, while the 6.8 nF capacitors simulate an approximately 500 Ω body impedance with the given frequency. The electrode model was omitted from the RA electrode due to practical reasons, since the series capacitance between two electrodes would affect the required capacitor value. Figure 24 shows the circuit for the electrode model.

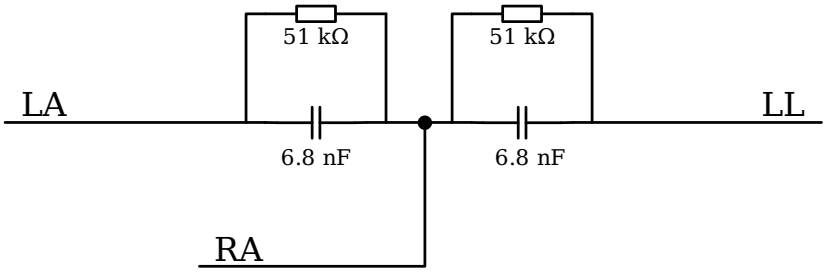

Figure 24: Electrode patient model circuit used in the EMI testing.

Test procedure

Prior to the testing, the generated electric field strength was calibrated at 2.5 meters for the required 3 V/m level throughout the frequency spectrum. The field uniformity at the test plane was confirmed with a field test probe. EUT was then placed on a nonconductive table in the anechoic chamber 2.5 meters from the field generation antenna. Normally, the test is performed with the field generating antenna facing each side of the EUT using a rotating table. Here, only two faces of the EUT were exposed to the field, as the selected faces were theoretically the worst in terms of the electromagnetic coupling. As it is possible to use the EUT in different orientations, both vertical and horizontal orientation were tested as required in IEC61000-4-3.

The field generating antenna was positioned at the same height as the EUT and the orientation of the antenna was set to either horizontal or vertical as required by the standard. The antenna orientations are shown in the Figure 25.

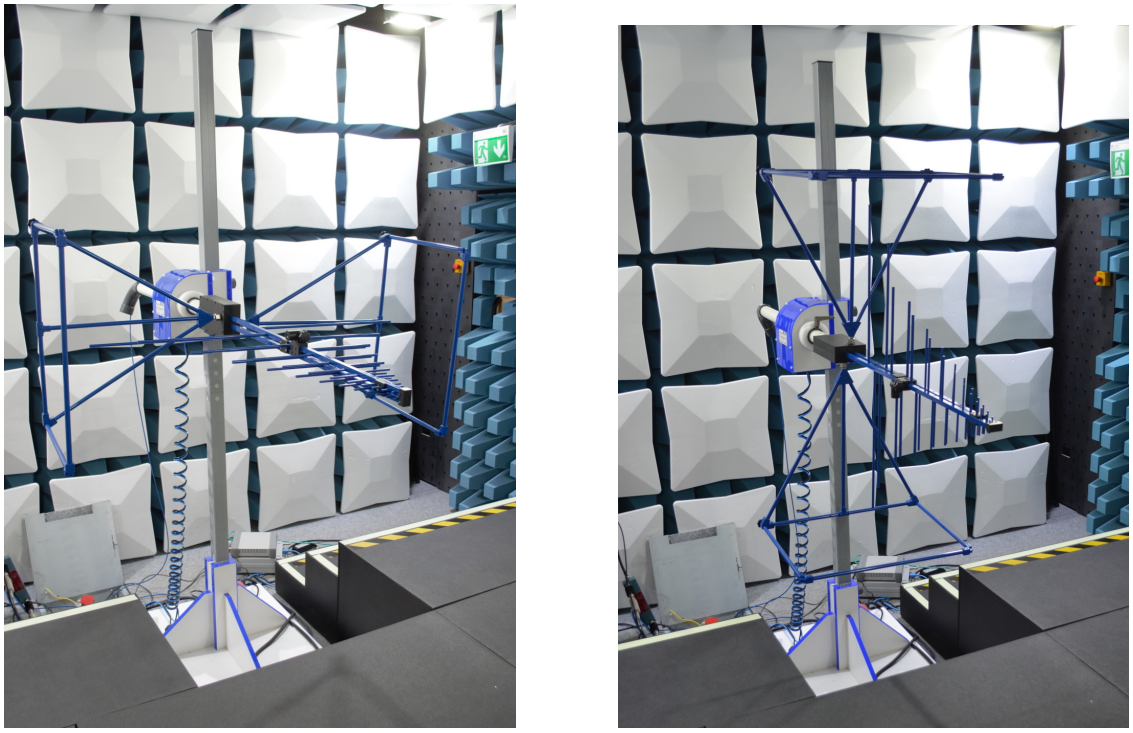

(a) Antenna in horizontal orientation.

(b) Antenna in vertical orientation.

Figure 25: Field generating antenna orientations.

After the antenna positioning, the field probe was positioned next to the EUT at the table, measuring the generated electric field strength during the tests. The receiving antenna for EUT measurement data was placed near the BLE radio module to ensure good signal strength. RF amplifier was powered on and the connection was checked from the test PC. Finally, the EUT was powered on and a short run of the biosignal measurement was tested from the data acquisition PC to ensure a good connection to the EUT.

The EMC test software (Rohde&Schwarz® Elektra 3.03) was configured to run a 2 Hz 80% amplitude modulated frequency sweep from 80 MHz to 1000 Mhz with 5 seconds dwell time for each frequency. IEC60601-1-2 states that the standard defined modulation frequency 1000 kHz can be changed if identified by the risk management process. The modulation frequency needs to be in the measurement range of the sensor. Thus, 2 Hz is a suitable choice as it fits into both ECG and RR sampling ranges. The frequency range was swept incrementally in 1% logarithmic steps. EUT acquisition was started, and the test began. A view of the complete measurement setup in the anechoic chamber can be seen in the Figure 26.

Figure 26: Test setup as seen from the anechoic chamber entrance. The field generating antenna can be seen in the background.

The test was repeated for each combination of antenna and EUT orientations. After the tests, resulting data was checked visually of any indication of interference. Additionally, spectrum analysis was used to verify the visual checks. If any of the test runs showed any interference in the data, that test was repeated concentrating on the frequency range where interference was present.

3.2.2 Proximity fields from RF wireless communications equipment

The proximity field immunity test follows closely the methodology used in radiated field immunity test in Section 3.2.1. However, these measurements have few key differences. The proximity of mobile communications immunity addresses the worst case of interference that a device could have to withstand from modern mobile communication devices. Since the standard required field strength for the test is 28 V/m, the test table is now moved to the distance of 1 meter from the field generating antenna. The field strength was carefully calibrated throughout the entire frequency range from 385 MHz to 1 GHz.

The test equipment was set up identically as with radiated field immunity tests except for the table is closer to the antenna. The frequency sweep was set up from 385 MHz to 1 GHz in logarithmic 1% increments with pulse modulation at 18 Hz with 50% duty cycle, following the test methodology defined in IEC61000-4-3.

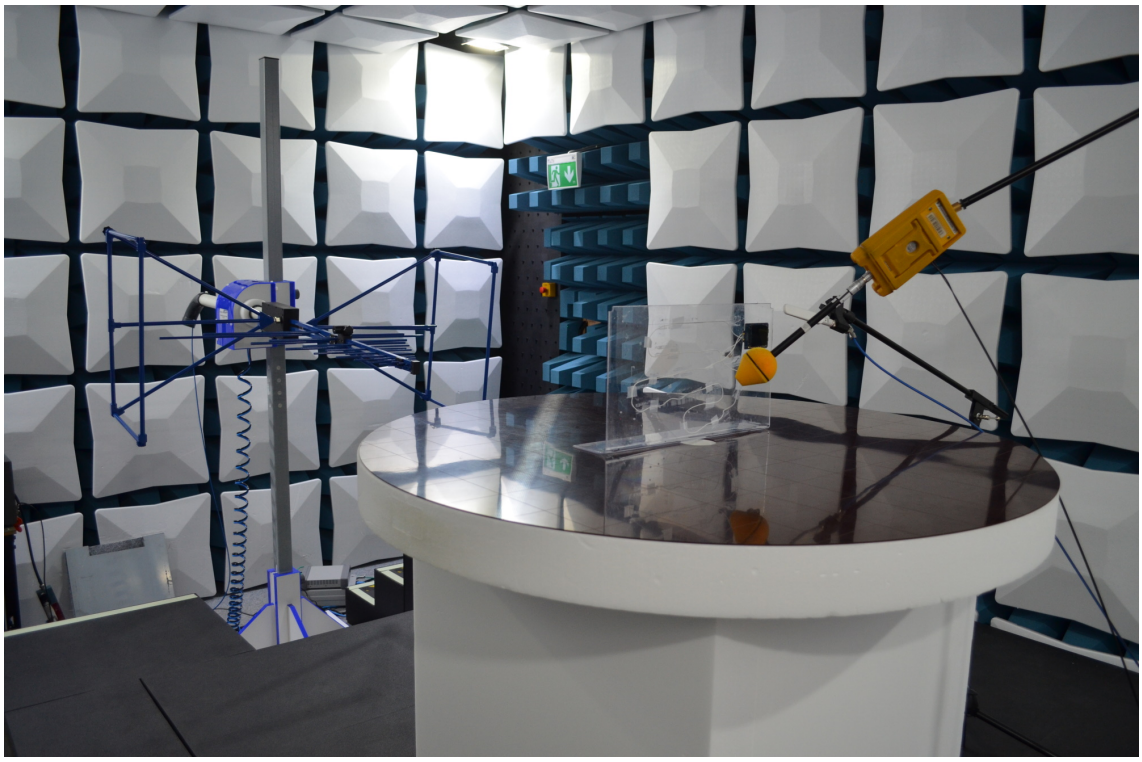

Figure 27: The proximity field immunity test setup. The test table is moved closer to the field generating antenna to enable reaching higher electric field strength with limited amplifier power.

3.2.3 Conducted disturbances induced by RF fields

Testing against frequencies below 80 MHz requires a special test setup. Essentially, this test simulates the same phenomena as the previous tests, but the interference is applied directly to the lead wires by current clamps. Conducted immunity testing simulates the normal voltage and current environment of auxiliary signal cables, in this case, the electrode lead wires. Bundled lead wires can have both capacitive and inductive coupling. The lead wire bundle is subjected to both common and differential mode disturbances with special current transducers or clamps.

The international collateral standard IEC 60601-1-2 requires testing the conducted disturbances in the “patient coupling port”, that is, all the cabling connected to the patient. In this case, the cables are three-electrode lead wires annotated as RA, LA, and LL. The EUT was placed on a nonconductive surface on a large conductive ground plane located in a special EMC test chamber. The complete test equipment setup is disclosed in Figure 28.

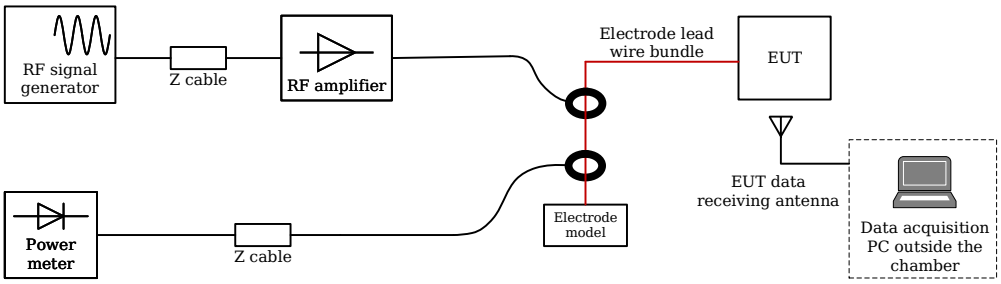

Figure 28: Test setup for the conducted disturbances immunity tests.

Current clamps were placed on the electrode cabling, one for injecting the current and one for measuring the current. The setup for the current clamps and the EUT lead wires can be seen in the Figure 29. As the RA electrode lead wire was very short (approximately 10 cm) it could not fit into the current inducing clamp. Therefore, the EUT was tested first in a differential configuration, leaving the RA lead wire out of the clamps. The common-mode configuration was tested by extending the RA lead wire so each wire could fit into the clamp setup.

IEC61000-4-6 Annex B allows reducing the injection current frequency bandwidth in respect to the length of the lead wires. Therefore, the test frequency band was selected to be 25 MHz–80 MHz in 1% logarithmic increments with 5 second dwell time. Modulation was set as 2 Hz 80% amplitude modulation. The EUT was connected to a similar electrode model to simulate electrode and patient impedance as with the radiated fields immunity tests. When the EUT was positioned in the clamp properly, the measurement was started.

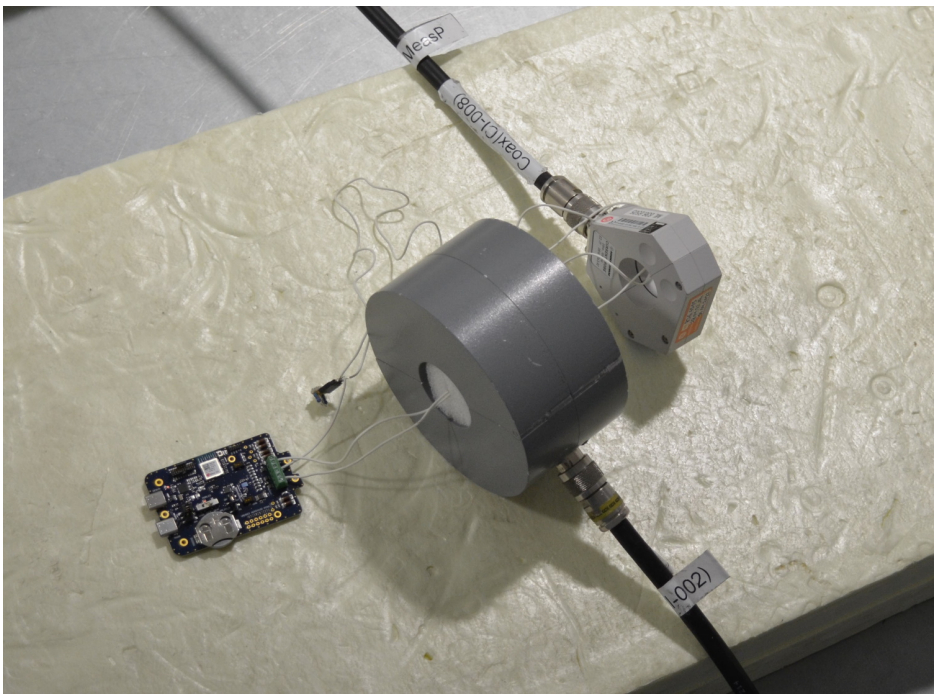

Figure 29: Lead wires in differential configuration inside the current clamp. Wires for LA and LL are fed through the current clamp as RA remains outside the loop.

3.2.4 Experiments to improve electromagnetic immunity

Based on the results of the EMI testing, several experimental configurations were tried to improve the EMI performance of the sensor front end. The effect of the experiments was evaluated by repeating the radiated and proximity EMI tests in certain selected orientations. Before these experiments, the coupling mechanism of the interference was tested by first shielding the EUT printed circuit board assembly (PCBA) to ensure that no interference was being picked up by the board itself. Then, the area of the lead wire bundle was changed to see if it affects the coupling frequency of the interference. It was found that by changing the area of the lead wire bundle, the frequency shifted as the resonant frequency of the loop "antenna" changed.

Filter capacitors

First experiments were done by placing additional filtering capacitors at the AFE inputs. It was expected that the capacitors at the AFE inputs would filter out high-frequency noise that couples to the front end. The value of the capacitors was restricted by the required measurement bandwidth and GPIO current drives. As previously shown in the Figure 21, the duration of the measurement time slots is only few microseconds which prohibits placing excessive capacitance to the input. The selected capacitor size for these experiments was 100 pF. First, differential capacitors were applied for RR channel TIA inputs. It was expected that if the interference is mostly differential, the differential capacitor would help in cancelling it.

Ground decoupled capacitors were also tested. Capacitors were placed to each TIA input pin for both ECG and RR. These capacitors could help by attenuating both common-mode and differential interference. However, ground decoupled capacitors affect negatively the CMRR, therefore differential capacitors are preferred if they turn out to be feasible. The GPIO current drives were also ground coupled to see if the interference has a path from GPIO pins to the supply voltage rails.

ECG isolation and reference voltage drive

ECG channel was isolated to see how much the RR measurement affects the total interference and if the ECG channel alone picks any interference. The isolation was done by removing the defibrillation resistors from the inputs of the unwanted signal and current lines. Therefore, the GPIO current drives and RR TIA channels were disconnected from the measurement circuit. Additionally, inner reference potential 0.9 V of the AFE was buffered and fed to the LA electrode. This basically ties the patient body to a set DC potential which could help to keep the signal baseline from drifting too close to the supply rails. However, this configuration was not possible with active IPG current drives, since it replaces the LA electrode current drive with the buffered DC voltage.

Shielded lead wires

EMI performance was also tested with shielded coaxial electrode lead wires to see how much they affect the total coupled interference. In theory, shielded lead wires should pick much less interference in general and we expected to see a major EMI performance improvement. However, shielded lead wires cannot solve issues if, for example, the impedance of the passive front end is unbalanced. Furthermore, shielded lead wires lead to more expensive, heavier, and bulkier solutions than with unshielded alternatives which can negatively affect the usability and even signal quality due to added strain to the electrode contacts.

4 Results

As the nature of electromagnetic interference is rather sporadic and arbitrary, there was variation within the test results. The actual mechanism for the coupling of the interference has not been indisputably proven and there could be various underlying mechanisms that contribute to the total interference seen at the measurement output. Some phenomena can be difficult to reproduce even with a seemingly identical setup. However, the standard requirements and the reference design form a coherent baseline for performance requirements, to which the results can be directly compared against.

This chapter presents all of the results related to electromagnetic immunity tests conducted with the dual-parameter prototype. This includes the initial EMI tests for the reference sensor and the dual-parameter prototype and also all of the modifications and improvements that were done throughout the testing. All of the three phenomena listed in Table 1 are addressed in their respective subsections. For the thorough test methodology, please refer to Sections 3.2.1 – 3.2.3. All of the resulting signals presented in this section have been filtered forward-backward with 1st order 40 Hz Butterworth lowpass filter for ECG and 1st order 20 Hz Butterworth lowpass filter for RR channels.

4.1 Radiated EM fields immunity

The conclusive results are gathered into a table which includes the results for each antenna and EUT orientation for both the dual-parameter prototype and the reference design. The most interesting findings are documented in graphical figures.

The overall numerical results presenting the peak-to-peak signal noise amplitudes for both the reference sensor and the dual-parameter prototype for each antenna and EUT orientation are presented in Table 2. The table presents the result cells with a colored background to indicate if the resulting values are in line with the requirements defined in Section 3.2 with a pass/fail sort of classification. Green indicates a pass, that is, the amplitude modulation of the test frequency sweep was not visible in the data and the overall peak-to-peak noise was within the acceptable range. Red indicates a failure, that is, there was a significant level of modulation visible in the measurement data.

EUT performed well in three antenna and EUT orientations with measurement consisting mostly of device internal noise. For the RR channels, approximately 1 Ω peak-to-peak noise was recorded in most orientations. The ECG channel performed well, and noise remained under 50 μV limit defined in the ECG standards.

However, with antenna and EUT in vertical orientation there was a significant amount of modulation visible in the measurement signal at around 180 MHz. The maximum amplitude of the modulation was 1.56 mV for ECG and 544 Ω for RR, which both by far exceeded the defined limits. Figure 30 shows the measurement results from vertical EUT and antenna orientation plotted throughout the frequency sweep from 80 MHz to 1 GHz, where the interference can be seen coupling to the measurement in each channel. The reference sensor did not show any signs of interference and the signals remained stable.

Table 2: Radiated EM fields immunity results for reference sensor and dual-parameter prototype. RR A corresponds lead RA – LL whereas RR B corresponds RA – LA.

Antenna orientation	EUT orientation	Channel	Reference	Prototype
Horizontal	Horizontal	ECG	4 μV	38 μV
		RR A	115 mΩ	2050 mΩ
		RR B	111 mΩ	1435 mΩ
	Vertical	ECG	4 μV	35 μV
		RR A	111 mΩ	972 mΩ
		RR B	101 mΩ	917 mΩ
Vertical	Horizontal	ECG	4 μV	37 μV
		RR A	115 mΩ	999 mΩ
		RR B	105 mΩ	871 mΩ
	Vertical	ECG	4 μV	1.56 mV
		RR A	120 mΩ	99.30 Ω
		RR B	114 mΩ	544.35 Ω

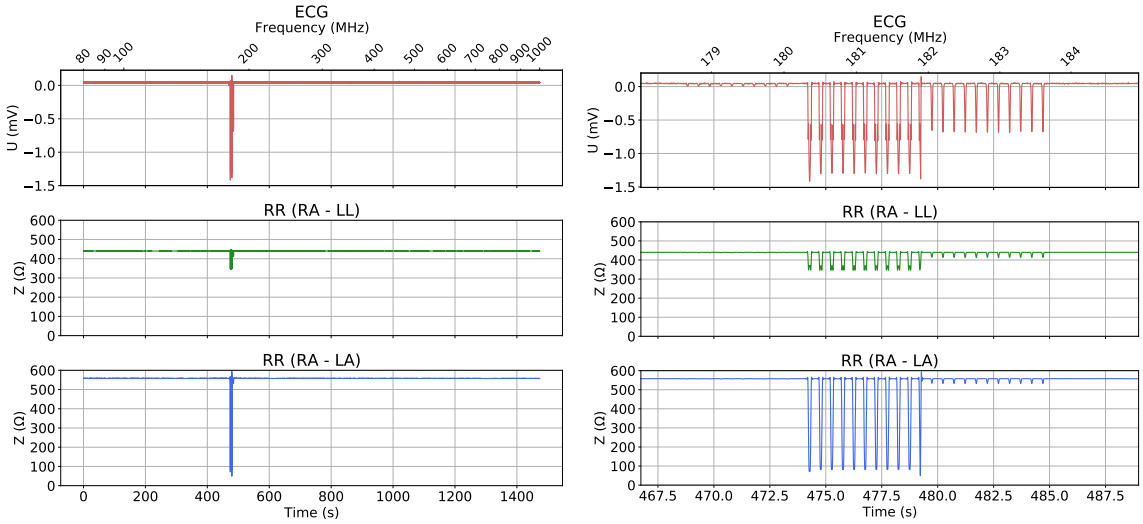

(a) The complete frequency sweep from 80 MHz to 1000 MHz.

(b) Zoomed view to the location of the interference.

Figure 30: Radiated emissions immunity test result with 3 V/m electric field strength antenna and EUT in vertical orientation. Interference visible at 180 MHz or at around 500 seconds mark.

4.2 Proximity fields from RF wireless communications equipment

Table 3 shows the results for the peak-to-peak interference in proximity fields immunity tests. EUT performed well with the antenna in a vertical orientation. Seemingly no interference was present in the measurement. However, the horizontal antenna orientation presented a real difficulty for the EUT. The extensive level shift was

caused through the frequency range from around 450 MHz to 500 MHz with ECG measuring maximum values at 4.7 mV and RR with 319 Ω. Also, the reference sensor did not show any signs of interference and the signals remained stable.

Table 3: Proximity RF EM fields immunity results. RR A corresponds lead RA – LL whereas RR B corresponds RA – LA.

Antenna orientation	EUT orientation	Channel	Reference	Prototype
Horizontal	Horizontal	ECG	234 μV	4.70 mV
		RR A	445 mΩ	56.07 Ω
		RR B	640 mΩ	317.05 Ω
	Vertical	ECG	6 μV	4.52 mV
		RR A	258 mΩ	55.57 Ω
		RR B	298 mΩ	319.19 Ω
Vertical	Horizontal	ECG	4 μV	32 μV
		RR A	235 mΩ	982 mΩ
		RR B	250 mΩ	1152 mΩ
	Vertical	ECG	10 μV	34 μV
		RR A	300 mΩ	893 mΩ
		RR B	514 mΩ	1175 mΩ

The measurement signals with visible interference can be seen in Figures 31 and 32. The interference is present at around 450–500 MHz for the horizontal EUT orientation and around 400–500 MHz for the vertical orientation.

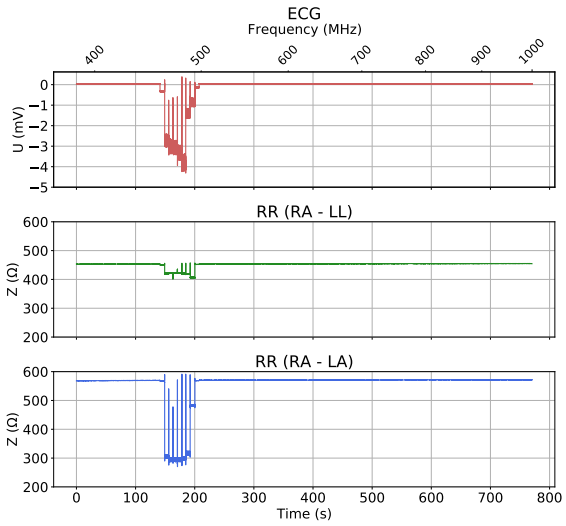

(a) The complete frequency sweep from 385 MHz to 1000 MHz.

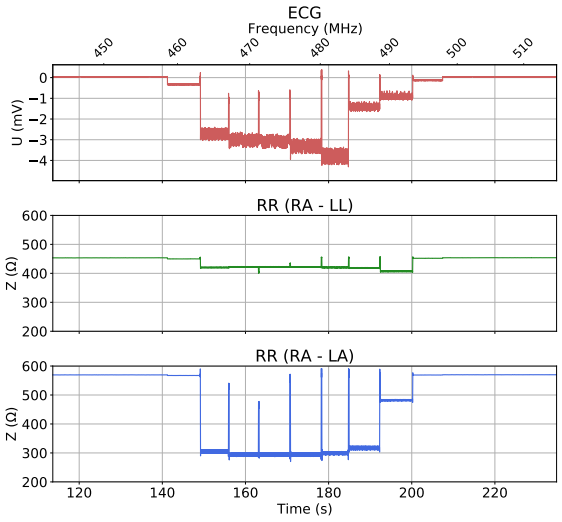

(b) Zoomed view to the location of the interference.

Figure 31: Interference coupling to the measurement with antenna and EUT in horizontal orientation for the proximity fields immunity test. The interference can be seen differing from the baseline noise at around 150 second mark or at around 470 MHz.

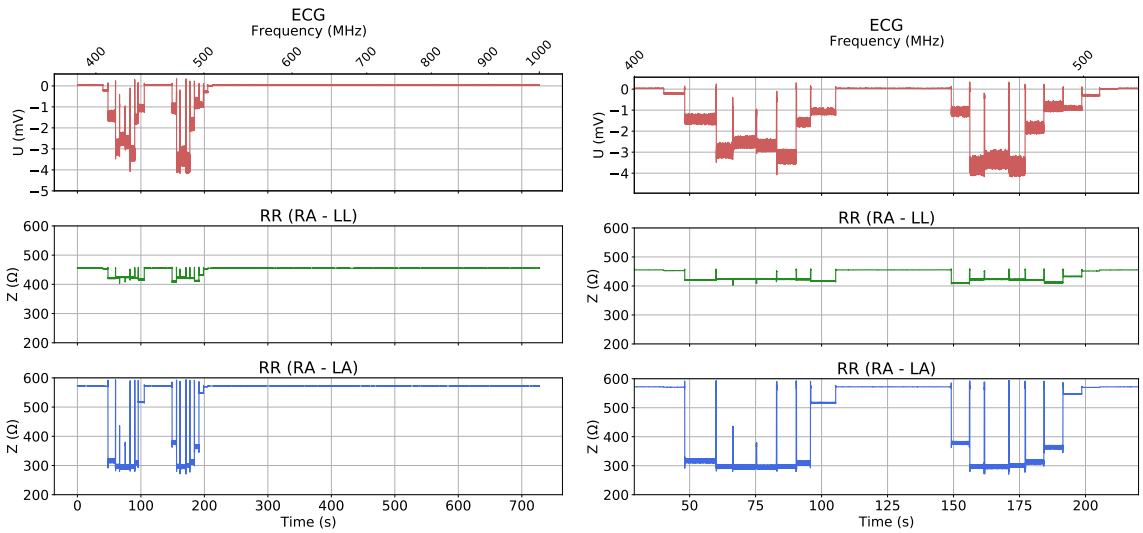

(a) The complete frequency sweep from 385 MHz to 1000 MHz.

(b) Zoomed view to the location of the interference.

Figure 32: Interference coupling to the measurement with antenna in horizontal and EUT in vertical orientation for the proximity fields immunity test. The interference can be seen differing from the baseline noise at around 50 second mark or at around 400 MHz.

4.3 Conducted disturbances induced by RF fields

Results for conducted disturbances induced by RF fields test are presented for both differential and common mode lead wire configurations in Table 4. For the dual-parameter prototype, the level of the maximum interference is similar in both differential and common mode lead wire configurations for RR measurement. For the ECG channel, the interference in differential configuration is almost six times higher. Looking at time-domain (Figures 33 and 34) plot of each test case, it becomes evident that the differential lead wire configuration is more prone to interference than with the common mode configuration. The reference sensor suffered from slight baseline drift in differential configuration, but the levels remained stable otherwise.

Table 4: Conducted immunity results. RR A corresponds lead RA – LL whereas RR B corresponds RA – LA.

Setup	Channel	Reference	Prototype
Differential	ECG	0.016 mV	19 mV
	RR A	0.752 Ω	118 Ω
	RR B	0.695 Ω	641 Ω
Common mode	ECG	0.004 mV	3 mV
	RR A	0.427 Ω	116 Ω
	RR B	0.414 Ω	595 Ω

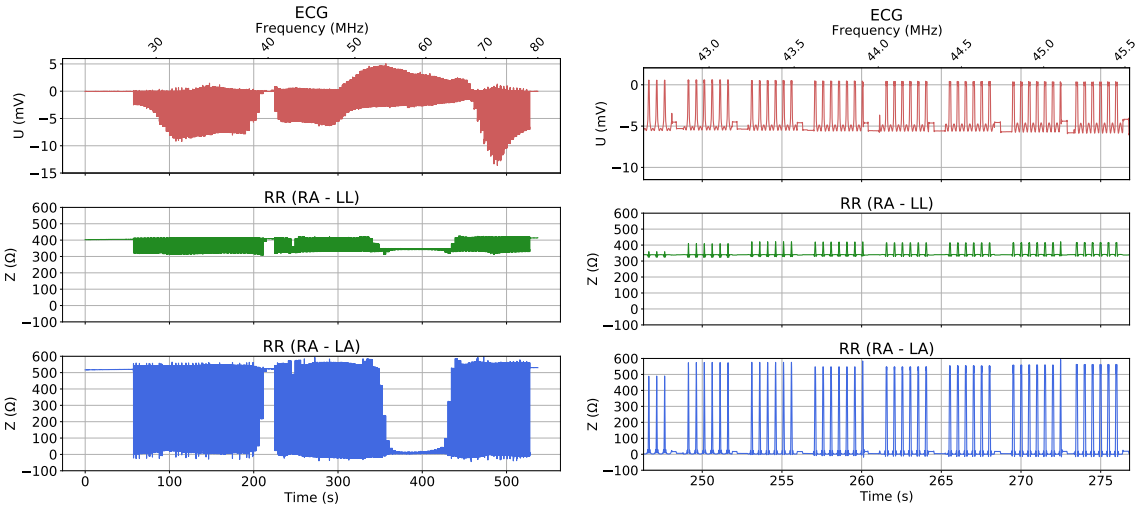

(a) The complete frequency sweep from 385 MHz to 1000 MHz.

(b) Zoomed view to the location of the interference.

Figure 33: Resulting interference in conducted disturbances immunity test with differential lead wire test configuration. A significant amount of interference can be seen almost throughout the frequency sweep.

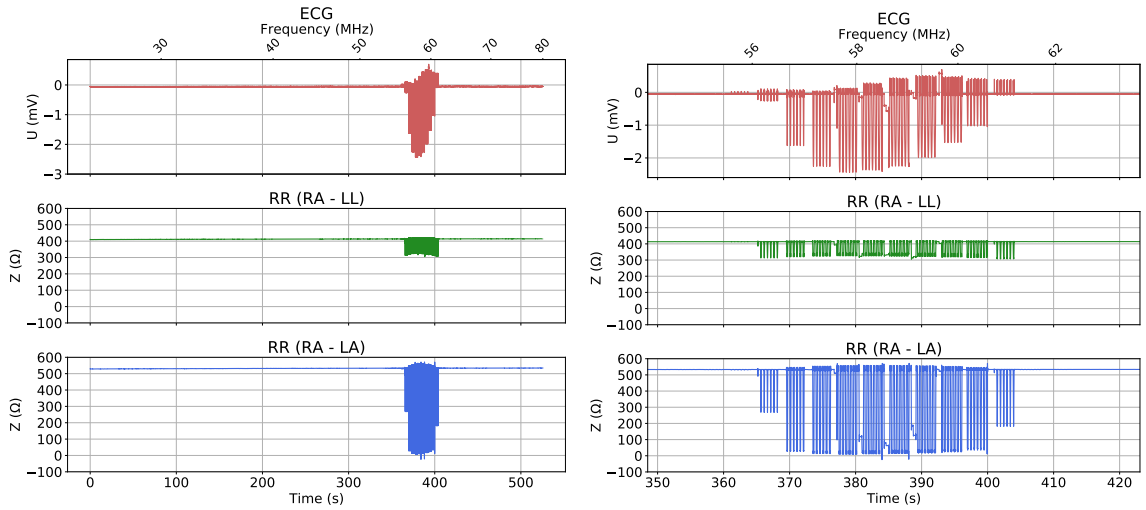

(a) The complete frequency sweep from 385 MHz to 1000 MHz.

(b) Zoomed view to the location of the interference.

Figure 34: Resulting interference in conducted disturbances immunity test with common mode lead wire test configuration. Interference is visible at around 60 MHz.

4.4 Wideband radiated and proximity interference

Wideband results for both radiated 3 V/m and proximity 28 V/m fields are presented in separate Tables 5 and 6. It should be also noted, that some data was lost around the 2.4 GHz frequency range because the radio communication between the prototype and the receiver was compromised.

The results for radiated wideband RF EM immunity with 3 V/m field and 2 Hz AM are good with no visible baseline shifting or modulation coupling in the measurements. However, for the proximity fields at 28 V/m and 217 Hz pulse modulation, there was a small level of baseline shifting and modulation coupling, which can be seen in the Figure 35. The coupling could be detected in various frequency bands with different antenna and EUT orientations producing different results. Again, the reference sensor performed well with no visible interference in the signal.

Table 5: Wideband RF EM radiated fields immunity results.

Antenna orientation	EUT orientation	Channel	Reference	Prototype
Horizontal	Horizontal	ECG	4.50 μV	33.15 μV
		RR A	110 mΩ	852 mΩ
		RR B	101 mΩ	1174 mΩ
	Vertical	ECG	3.94 μV	32.75 μV
		RR A	107 mΩ	1083 mΩ
		RR B	89 mΩ	868 mΩ
Vertical	Horizontal	ECG	3.97 μV	34.08 μV
		RR A	100 mΩ	893 mΩ
		RR B	91 mΩ	699 mΩ
	Vertical	ECG	3.71 μV	33.91 μV
		RR A	103 mΩ	761 mΩ
		RR B	90 mΩ	681 mΩ

Table 6: Wideband RF EM proximity fields immunity results.

Antenna orientation	EUT orientation	Channel	Reference	Prototype
Horizontal	Horizontal	ECG	502 μV	46.01 μV
		RR A	153 mΩ	1835 mΩ
		RR B	115 mΩ	943 mΩ
	Vertical	ECG	4.82 μV	37.47 μV
		RR A	121 mΩ	1767 mΩ
		RR B	95 $m\Omega$	1152 mΩ
Vertical	Horizontal	ECG	4.43 μV	33.01 μV
		RR A	103 mΩ	790 mΩ
		RR B	97 mΩ	1034 mΩ
	Vertical	ECG	4.68 μV	29.33 μV
		RR A	121 mΩ	893 mΩ
		RR B	91 mΩ	1370 mΩ

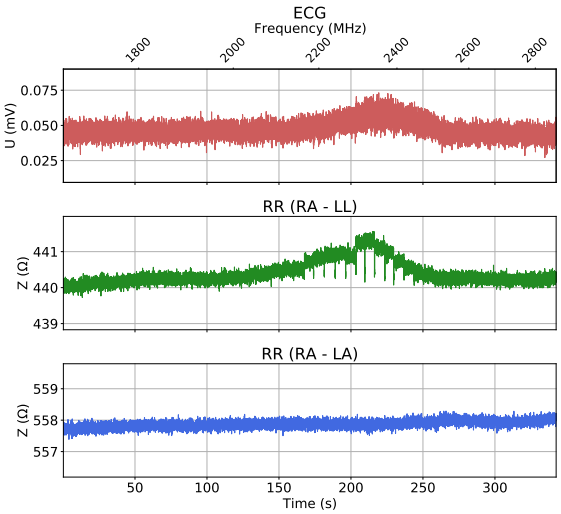

(a) Antenna and EUT in horizontal orientation

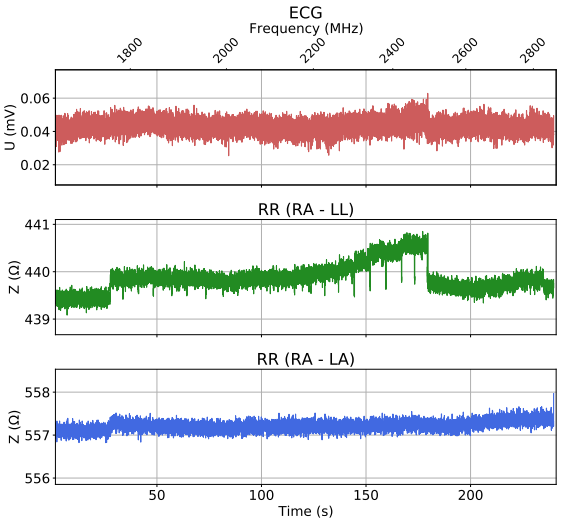

(b) Antenna in horizontal and EUT in vertical orientation

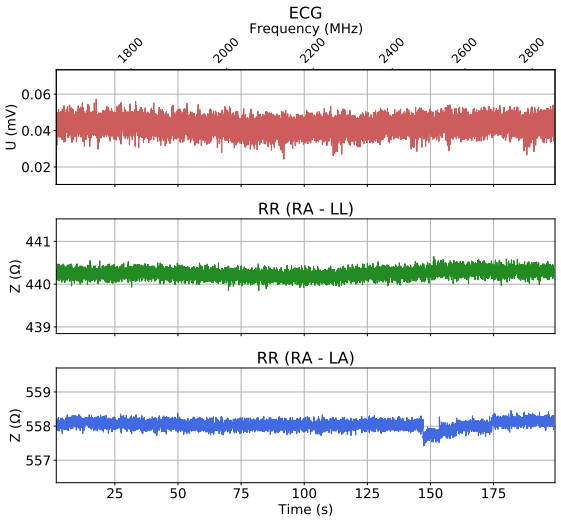

(c) Antenna in vertical and EUT in horizontal orientation

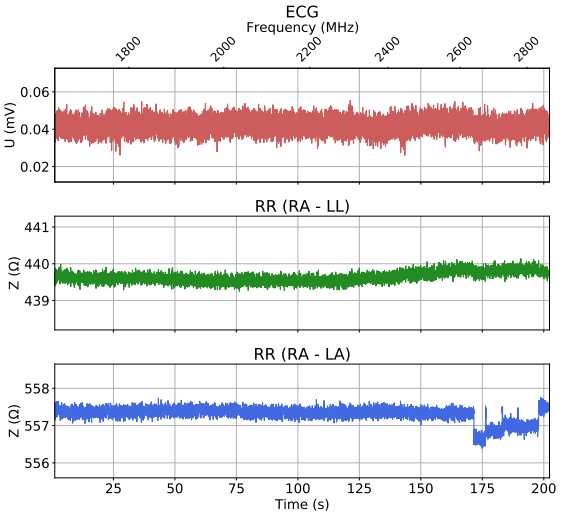

(d) Antenna and EUT in vertical orientation

Figure 35: Small level of interference seen in RR channels in wideband proximity immunity tests in every orientation. The level of the interference is around 2 Ω at worst, exceeding our limit of 100 mΩ peak-to-peak.

4.5 Experiments to improve EMI performance

As shown in the previous sections, the analog front end is not feasible considering the electromagnetic immunity standard compliance. Based on the results, few additional modifications were tested to see if the EMI performance could be improved within the set front-end configuration. The effect of the experiments was evaluated in radiated and proximity EMI test in the orientations the interference was found prominent. The results of these experiments are described in the following Table 7.

Table 7: EMI performance enhancement results table for radiated immunity test. Antenna in vertical and EUT in vertical orientation.

Description of the experiment	**Result**	**Conclusion**
Differential capacitor between TIA inputs of RR channels	ECG = 836 μV RR A = 99.27 Ω RR B = 297.80 Ω	The differential capacitors reduced the level of interference slightly, but the overall level of the interference remained high
Ground decoupled capacitors at GPIO current drives	ECG = 872 μV RR A = 94.17 Ω RR B = 131.99 Ω	Ground decoupling at GPIO pins reduced the interference level at RR B channel, but the overall effect was small
Ground decoupled capacitors at GPIO current drives and differential capacitors between TIA inputs of RR channels	ECG = 852 μV RR A = 110.97 Ω RR B = 140.47 Ω	Combined TIA differential decoupling together with GPIO decoupling provided no benefit when compared to decoupling only GPIO's
Ground decoupled capacitors at GPIO current drives and ground decoupled capacitors at TIA inputs of RR channels	ECG = 221 μV RR A = 39.05 Ω RR B = 38.51 Ω	Adding ground decoupling to the TIA inputs helped reducing the level of interference, but the remaining interference was still prominent
Isolated ECG channel with RR measurement disabled	ECG = 614 μV RR A = no data RR B = no data	Isolating the ECG channel did not have any significant effect to the interference levels at ECG channel
Isolated ECG channel with 0.9 V driven to the LA electrode	ECG = 30 μV RR A = no data RR B = no data	Driving the LA to 0.9 V reference stabilized the ECG channel with seemingly no interference present in ECG
Shielded lead wires with default front end configuration	ECG = 35 μV RR A = 1.23 Ω RR B = 1.32 Ω	Shielded lead wires completely eliminated the interference in every channel

The modifications were also evaluated in proximity fields immunity tests at 28 V/m electric field strength, where the findings were similar to the Table 7. However, with 28 V/m proximity fields, the isolated ECG channel with 0.9 V LA drive still had a small level of interference visible. It seems, that the 0.9 V drive at this configuration cannot improve the immunity beyond a certain level. Furthermore, while the tests in proximity fields also showed very good immunity using shielded lead wires, there was still a small amount of interference left at the beginning of the sweep at 385 MHz. Therefore, the interference could not be completely eliminated for proximity fields immunity tests.

5 Discussion

In this thesis, a new method of measuring ECG and RR was studied using a small wireless sensor prototype based on the ADPD4100 multimodal analog sensor front end. The passive sensor front end and the novel measurement principle for sequential ECG and RR was designed and simulated as a group effort with the help of engineers from GE Healthcare Finland and Analog Devices, Inc. A prototype of the wireless sensor was designed at GE Healthcare Finland along with the sensor software. The prototype was used to evaluate the overall performance of the front end considering the noise performance, biosignal quality and strength, and to gain more understanding of the versatile configuration options of ADPD4100. The main use for the ECG and RR sensor prototype was to test the electromagnetic immunity of the sensor front end against the EMC standard requirements.

The prototype performed well in the biosignal acquisition test. When using the vital signs simulator, the set signal amplitudes were correctly represented in the measurement. ECG could be measured with good precision from both simulator and live subject. Impedance based respiration signal was clearly visible in both simulator and live subject tests and would be feasible for determining at least a resting RR.

The initial noise level of the sensor prototype was higher than expected. The peak-to-peak noise for RR was measured at 70–150 mΩ whereas respiration caused impedance changes can be as low as 100 mΩ. Therefore, if the noise floor is too high, small respiration signals could be buried in the noise and remain undetected. Both channels suffered from unknown noise components at multiples of 30 Hz. The source of the noise could not be identified during the work, but it was considered that their presence does not affect proceeding with the EMC testing. The noise components were not seen in measurements using ADI evaluation board.

The development of the sensor software turned out to be a more challenging task than initially expected. Tuning the measurement timings, acquisition parameters and going through the numerous registers of ADPD4100 required extensive group effort. However, this gave us important insight into the core functionalities of the AFE and makes the future development of the sensor more straightforward.

The prototype along with a set of lead wires with electrode skin contact impedance model was subjected to a set of standard required electromagnetic immunity tests, that is, radiated RF EM fields at 3 V/m and 28 V/m and conducted disturbances induced by RF fields at 3 V/m. The performance was compared to a standard compliant reference sensor with more traditional parallel continuous ECG and RR measurement, whose EMC characteristics were also recorded during the tests. Initially, the passive sensor front end was equipped with minimal filtering components to achieve the best signal quality. However, the results of the initial EMC tests showed that the sensor front end is susceptible to interference in certain frequency ranges. The interference level could be measured at hundreds of ohms for RR and few millivolts for ECG. This made the comparison to the reference sensor unavailing since no proper comparison could be done due to the excessive interference. The reference sensor did not show any notable signs of interference.

Reproducing the exact interference during the multiple test runs was challenging

at times. For example, the interference observed in radiated EM fields test with 3 V/m electric field strength was difficult to reproduce every time. The interference was seen only in a very narrow frequency band and the positioning and angling of the EUT in respect to the field generating antenna could make a difference if the interference was seen at all. Interference in proximity and conducted immunity tests were easy to reproduce as the electric field strengths were so high.

Several actions were attempted for attenuating the amplitude of the interference. Adding differential capacitors to the RR channel TIA inputs had no significant positive effect to the level of interference. However, ground-coupled capacitors showed some promise by reducing the level of interference by some tens of ohms in RR channels. Decoupling both the GPIO current drives and RR at TIA inputs was found to be the most effective configuration. However, the effect of the decoupling did was rather negligible considering the overall magnitude of the interference, and the interference levels remained high and far beyond the set limits.

In one test setup, the ECG channel was isolated from the rest of the passive circuit to see if it alone picks up the same level of interference. The interference remained prominent also with isolated ECG. The prototype board was equipped with an option to drive the LA electrode to 0.9 V reference voltage, effectively tying the patient body to the set DC potential. This option was found very effective in reducing the interference in ECG, with only a small level of interference leaking through. Unfortunately, this configuration could not be used together with active RR measurement, so it only provided a partial solution for the isolated ECG measurement.

Finally, the sensor prototype was equipped with shielded coaxial electrode cables instead of the unshielded counterpart. The interference was completely eliminated, excluding some corner cases with 28 V/m field strengths. The effect of the shielded cables was so drastic that it became evident, this design at this stage would not be feasible without them. The EMC performance without shielded cables was not even comparable with the reference sensor with simultaneous frequency-based ECG and RR with unshielded electrode cables. Based on the results, shielded lead wires would seem as the obvious choice. However, they increase the cost of the system and hamper usability because of the heavier wires. Added weight also increases the stress at the electrode contacts, which can negatively affect the signal quality.

The hypothesis was, that the laid-out model of the patient electrode cables was acting as a receiving antenna for the detected interference frequency band. This was especially evident since by changing the orientation of the field generating antenna and/or the electrode cable assembly to certain orientations, the interference would disappear completely. Additionally, switching to shielded lead wires also eliminated the interference. To further ensure the hypothesis, the EUT PCBA was shielded using tin foil, which did not make a difference considering the interference. The phenomenon was also studied by making changes to the area and tightness of the electrode cable loops, which was shown to affect the interference coupling by shifting the coupling frequency or entirely eliminating it altogether. These findings bring up another aspect when considering the form factor of the sensor. The current prototype is equipped with lengthy, approximately 40 cm long lead wires intended for reach the standard electrode positions RA, LA, and LL. Reducing the length of the lead wires

and bringing them closer together would effectively reduce the overall area of the sensor assembly. This approach is used in some disposable sensor patches, such as already mentioned Philips BX100. The reduced overall area of the cabling increases the resonant frequency of the "antenna". A higher frequency interference would be much easier to filter out with the input capacitors, which in turn would improve the electromagnetic immunity of the front end.

It can be concluded that meeting the EMC standard compliancy with ADPD4100 still requires a lot of work. We learned that time-based multiplexing brings special challenges with optimizing the timings for integration of the measurement signals for optimal biosignal quality. Additionally, alleviating the interference with passive input filtering is not feasible for such prominent levels of interference. Multiplexing the different types of signals requires wide bandwidth, preventing of adding excessive capacitance to the TIA inputs. Additional filtering is a trade-off between signal quality and the interference levels. Furthermore, the input filtering can have a negative effect on the signal quality and especially on the high-frequency current drives, as some amount of current is leaked to the ground through the capacitors. Driving the body to a certain reference voltage can be a partial solution to improve the electromagnetic immunity of the front end but combining it with the RR measurement requires a specifically designed circuit. Shielded lead wires improve the immunity significantly, but it is not a perfect solution due to the negative impact on the cost and usability of the system.

Currently, the EMC performance of the ADPD4100 for ECG and RR measurement could reach standard-compliant levels with minor modifications, provided that shielded lead wires are used. If the goal is to use long, non-shielded lead wires, a new design round for the AFE component might be required. Based on the tests with different sized lead wire bundles, unshielded lead wires could be feasible in a "sensor patch" type of application with significantly reduced lead wire lengths.

In addition to the EMC results, this work examined the feasibility of the proposed design for dual- or multiparameter disposable sensors. The findings in the work including the PCBA design process, software development, ADPD4100 configuration options, EMC findings, and the effect of passive filtering have been valuable for the entire team by mapping out the critical pitfalls that may have been found out only later during the product development. The developed prototype functions as a wearable and wireless proof of concept of an ECG and RR sensor and therefore can be used in future research projects, such as in usability studies or in other types of electromagnetic compatibility testing.

References

Ackmann, J. and Seitz, M. (1984). "Methods of complex impedance measurements in biologic tissue". In: Critical Reviews In Biomedical Engineering, pp. 281–311.

Adler, A., Guardo, R., and Berthiaume, Y. (1996). "Impedance imaging of lung ventilation: do we need to account for chest expansion?" *IEEE Transactions on Biomedical Engineering* 43.4, pp. 414–420. ISSN: 1558-2531. DOI: 10.1109/10.486261.

Al-Khalidi, F., Saatchi, R., Burke, D., Elphick, H., and Tan, S. (2011). "Respiration rate monitoring methods: A review". *Pediatric Pulmonology* 46.6, pp. 523–529. ISSN: 1099-0496. DOI: 10.1002/ppul.21416.

Analog Devices, Inc. (2020). "ADPD4100 Datasheet and Product Info". Available at: https://www.analog.com/en/products/adpd4100.html (Accessed: 12/14/2020).

Armitage, M., Eddleston, J., and Stokes, T. (2007). "Recognising and responding to acute illness in adults in hospital: summary of NICE guidance". *BMJ : British Medical Journal* 335.7613, pp. 258–259. ISSN: 0959-8138. DOI: 10.1136/bmj.39272.679688.47.

Baker, L., Geddes, L. A., Hoff, H. E., and Chaput, C. J. (1966). "Physiological factors underlying transthoracic impedance variations in respiration." *Journal of Applied Physiology*. DOI: 10.1152/jappl.1966.21.5.1491.

Bates, A., Ling, M. J., Mann, J., and Arvind, D. K. (2010). "Respiratory Rate and Flow Waveform Estimation from Tri-axial Accelerometer Data". In: Proceedings of 2010 International Conference on Body Sensor Networks. ISSN: 2376-8894, pp. 144–150. DOI: 10.1109/BSN.2010.50.

Becchetti, C. and Neri, A. (2013). *Medical Instrument Design and Development: From Requirements to Market Placements*. John Wiley & Sons, Incorporated. 445 pp. ISBN: 978-1-118-65246-6.

Bergese, S. D., Mestek, M. L., Kelley, S. D., McIntyre, R., Uribe, A. A., Sethi, R., Watson, J. N., and Addison, P. S. (2017). "Multicenter Study Validating Accuracy of a Continuous Respiratory Rate Measurement Derived From Pulse Oximetry: A Comparison With Capnography". *Anesthesia and Analgesia* 124.4, pp. 1153–1159. ISSN: 0003-2999. DOI: 10.1213/ANE.0000000000001852.

Bit-Babik, G., Morrissey, J. J., Faraone, A., and Balzano, Q. (2007). "Electromagnetic compatibility management of wireless transceivers in electromagnetic-interference-sensitive medical environments". *Annali dell'Istituto Superiore Di Sanita* 43.3, pp. 218–224. ISSN: 0021-2571.

Brown, B. H., Barber, D. C., Morice, A. H., and Leathard, A. D. (1994). "Cardiac and respiratory related electrical impedance changes in the human thorax". *IEEE Transactions on Biomedical Engineering* 41.8, pp. 729–734. ISSN: 1558-2531. DOI: 10.1109/10.310088.

Bunkenborg, G., Poulsen, I., Samuelson, K., Ladelund, S., and Akeson, J. (2019). "Bedside vital parameters that indicate early deterioration". *International Journal of Health Care Quality Assurance* 32.1. Publisher: Emerald Publishing Limited, pp. 262–272. ISSN: 0952-6862. DOI: 10.1108/IJHCQA-10-2017-0206.

Clayton, G. B. and Winder, S. (2003). *Operational Amplifiers*. Jordan Hill, United Kingdom: Elsevier Science & Technology. ISBN: 978-0-08-047982-8.

Coccolini, F., Perrone, G., Chiarugi, M., Di Marzo, F., Ansaloni, L., Scandroglio, I., Marini, P., Zago, M., De Paolis, P., and Forfori, F. (2020). "Surgery in COVID-19 patients: operational directives". *World Journal of Emergency Surgery* 15. Publisher: Springer, pp. 1–7. DOI: 10.1186/s13017-020-00307-2.

Cretikos, M. A., Bellomo, R., Hillman, K., Chen, J., Finfer, S., and Flabouris, A. (2008). "Respiratory rate: the neglected vital sign". *The Medical Journal of Australia* 188.11, pp. 657–659. DOI: 10.5694/j.1326-5377.2008.tb01825.x.

Duan, N., Gao, W., and Wang, Q. (2020). "Preparedness and disinfection of anesthetic equipment in COVID-19". *Journal of Clinical Anesthesia* 66. Publisher: Elsevier, p. 109924. DOI: 10.1016/j.jclinane.2020.109924.

Elliott, M. and Coventry, A. (2012). "Critical care: the eight vital signs of patient monitoring". *British Journal of Nursing* 21.10. Publisher: Mark Allen Group, pp. 621–625. ISSN: 0966-0461. DOI: 10.12968/bjon.2012.21.10.621.

Fieselmann, J. F., Hendryx, M. S., Helms, C. M., and Wakefield, D. S. (1993). "Respiratory rate predicts cardiopulmonary arrest for internal medicine inpatients". *Journal of General Internal Medicine* 8.7, pp. 354–360. DOI: 10.1007/BF02600071.

Gabriel, S., Lau, R. W., and Gabriel, C. (1996). "The dielectric properties of biological tissues: III. Parametric models for the dielectric spectrum of tissues". *Physics in Medicine & Biology* 41.11. Publisher: IOP Publishing, p. 2271. ISSN: 0031-9155. DOI: 10.1088/0031-9155/41/11/003.

GE Healthcare (2020). *The whole world started calling, asking for monitors!* Available at: https://www.gehealthcare.fi/article/the-whole-world-started-calling-asking-for-monitors (Accessed: 05/31/2021).

Goldberger, A. L., Goldberger, Z. D., and Shvilkin, A. (2018). *Goldberger's Clinical Electrocardiography: A Simplified Approach*. Edition: Ninth edition. ISBN: 9780323508773 Place: Philadelphia, PA. Elsevier.

Gravenstein, J. S., Jaffe, M. B., Gravenstein, N., and Paulus, D. A. (2011). *Capnography*. Cambridge, United Kingdom: Cambridge University Press. ISBN: 978-0-511-92799-7. DOI: 10.1017/CBO9780511933837.

Grimnes, S. and Martinsen, Ø. G. (2015). *Bioimpedance and Bioelectricity Basics*. 3rd edition. Elsevier. ISBN: 978-0-12-411470-8. DOI: 10.1016/C2012-0-06951-7.

GSMA (2020). *The Mobile Economy*. Available at: https://www.gsma.com/mobileeconomy/ (Accessed: 04/16/2021).

Gupta, R., Mitra, M., and Bera, J. (2013). *ECG Acquisition and Automated Remote Processing*. ISBN: 9788132215578 Place: New Delhi. Springer. ISBN: 978-81-322-1557-8. DOI: 10.1007/978-81-322-1557-8.

Houtveen, J. H., Groot, P. F. C., and Geus, E. J. C. (2006). "Validation of the thoracic impedance derived respiratory signal using multilevel analysis". *International Journal of Psychophysiology* 59.2, pp. 97–106. ISSN: 0167-8760. DOI: 10.1016/j.ijpsycho.2005.02.003.

IEC 60601-1 (2020). *Medical Electrical Equipment – Part 1: General Requirements for Basic Safety and Essential Performance*. Edition 3.2. International Electrotechnical Commission.

IEC 60601-1-2 (2020). *Medical Electrical Equipment – Part 1-2: General Requirements for Basic Safety and Essential Performance – Collateral Standard: Electromagnetic Disturbances – Requirements and Tests*. Edition 4.1. International Electrotechnical Commission.

IEC 60601-1-2-27 (2011). *Medical Electrical Equipment – Part 2-27: Particular Requirements for the Basic Safety and Essential Performance of Electrocardiographic Monitoring Equipment*. Edition 3.0. International Electrotechnical Commission.

IEC 61000-4-3 (2020). *Electromagnetic Compatibility (EMC) – Part 4-3: Testing and Measurement Techniques – Radiated, Radio-Frequency Electromagnetic Field Immunity Test*. Edition 4.0. International Electrotechnical Commission.

IEC 61000-4-6 (2013). *Electromagnetic Compatibility (EMC) – Part 4-6: Testing and Measurement Techniques – Immunity to Conducted Disturbances, Induced by Radio-Frequency Fields*. Edition 4.0. International Electrotechnical Commission.

IEC 80601-2-49 (2018). *Medical Electrical Equipment – Part 2-49: Particular Requirements for the Basic Safety and Essential Performance of Multifunction Patient Monitors*.

Kaiser, K. L. (2004). *Electromagnetic Compatibility Handbook*. CRC Press. 2730 pp. ISBN: 978-0-8493-2087-3.

Kelly, C. (2018). *Respiratory rate 1: why measurement and recording are crucial*. Nursing Times. Available at: https://www.nursingtimes.net/clinical-archive/respiratory-clinical-archive/respiratory-rate-1-why-measurement-and-recording-are-crucial-26-03-2018/ (Accessed: 01/26/2021).

Malmivuo, J. and Plonsey, R. (1995). *Bioelectromagnetism - Principles and Applications of Bioelectric and Biomagnetic Fields*. New York, NY. Available at: https://www.bem.fi/book/ (Accessed: 01/20/2021).

Martindale, J. L. and Brown, D. F. M. (2017). *A Visual Guide to ECG Interpretation*. Edition: Second edition. ISBN: 9781496365712 Place: Philadelphia. Wolters Kluwer.

McBride, J., Knight, D., Piper, J., and Smith, G. B. (2005). "Long-term effect of introducing an early warning score on respiratory rate charting on general wards". *Resuscitation* 65.1, pp. 41–44. ISSN: 0300-9572. DOI: 10.1016/j.resuscitation.2004.10.015.

Młyńczak, M. and Cybulski, G. (2012). "Impedance pneumography: Is it possible?" *SPIE - The International Society for Optical Engineering 8454*. DOI: 10.1117/12.2000223.

Ott, H. W. (2009). *Electromagnetic Compatibility Engineering*. ISBN: 9780470508503 Place: Hoboken, N.J. John Wiley & Sons, Incorporated. ISBN: 978-0-470-50850-3. DOI: 10.1002/9780470508510.

Pamula, V. R., Hoof, C., and Verhelst, M. (2019). *Analog-and-Algorithm-Assisted Ultra-Low Power Biosignal Acquisition Systems*. Analog circuits and signal processing series. ISBN: 9783030058708 Series: Analog circuits and signal processing series. Cham, Switzerland: Springer Nature. ISBN: 978-3-030-05870-8.

Philips (2021). *Biosensor BX100*. Available at: http://www.usa.philips.com/en/healthcare/product/HC989803203011/biosensor-bx100-wearable-remote-measurement-device (Accessed: 07/07/2021).

Ramsay, M. A. E., Usman, M., Lagow, E., Mendoza, M., Untalan, E., and De Vol, E. (2013). "The accuracy, precision and reliability of measuring ventilatory rate and detecting ventilatory pause by rainbow acoustic monitoring and capnometry". *Anesthesia and Analgesia* 117.1, pp. 69–75. ISSN: 1526-7598. DOI: 10.1213/ANE.0b013e318290c798.

Redmond, C. (2013). *Transthoracic Impedance Measurements in Patient Monitoring*. Available at: https://www.analog.com/en/technical-articles/transthoracic-impedance-measurements-in-patient-monitoring.html (Accessed: 02/15/2021).

Retory, Y., Niedzialkowski, P., Picciotto, C. de, Bonay, M., and Petitjean, M. (2016). "New Respiratory Inductive Plethysmography (RIP) Method for

Evaluating Ventilatory Adaptation during Mild Physical Activities". *PLoS ONE* 11.3. ISSN: 1932-6203. DOI: 10.1371/journal.pone.0151983.

Ryan, H., Cadman, C., and Hann, L. (2004). "Setting standards for assessment of ward patients at risk of deterioration". *British Journal of Nursing* 13.20. Publisher: Mark Allen Group, pp. 1186–1190. ISSN: 0966-0461. DOI: 10.12968/bjon.2004.13.20.17008.

Sensium Healthcare Ltd. (2020). *Sensium | Early detection of patient deterioration.* Sensium | Early detection of patient deterioration. Available at: https://www.sensium.co.uk/us/. (Accessed: 07/07/2021).

Silva, F., Fernández-Chimeno, M., and Pallas-Areny, R. (1994). "Fluorescent lights interferences on high resolution ECG". In: Proceedings of XVII World Congress on Medical Physics and Biomedical Engineering. Rio de Janeiro, Brazil, 257, paper OS11–4.6.

Sörnmo, L. and Laguna, P. (2015). *Bioelectrical Signal Processing in Cardiac and Neurological Applications.* 1st ed. Elsevier. 688 pp. ISBN: 978-0-12-437552-9. DOI: 10.1016/B978-0-12-437552-9.X5000-4.

Tagawa, T., Tamura, T., and Oberg, P. A. (2011). *Biomedical Sensors and Instruments.* Baton Rouge: Taylor & Francis Group, CRC Press. ISBN: 978-1-4200-9078-9.

Thaler, M. (2019). *The Only EKG Book You'll Ever Need.* 9th ed. Philadelphia: Wolters Kluwer, Lippincott Williams & Wilkins. ISBN: 978-1-4963-7723-4.

Thompson, B. R., O'Hehir, R. E., and Borg, B. M. (2014). *Spirometry.* Chichester, United Kingdom: John Wiley & Sons, Incorporated, pp. 13–36. ISBN: 9781118405512. DOI: 10.1002/9781118405444.ch2.

Tortora, G. J. and Derrickson, B. H. (2017). *Tortora's Principles of Anatomy and Physiology, 15th Edition.* John Wiley & Sons, Incorporated. ISBN: 978-1-119-40006-6.

Vincent, J.-L., Einav, S., Pearse, R., Jaber, S., Kranke, P., Overdyk, F. J., Whitaker, D. K., Gordo, F., Dahan, A., and Hoeft, A. (2018). "Improving detection of patient deterioration in the general hospital ward environment". *European Journal of Anaesthesiology* 35.5, pp. 325–333. ISSN: 0265-0215. DOI: 10.1097/EJA.0000000000000798.

Webster, J. G. and Nimunkar, A. J. (2020). *Medical Instrumentation: Application and Design.* 5th Edition. John Wiley & Sons, Incorporated. ISBN: 978-1-119-45733-6.

Wheatley, I. (2018). *Respiratory rate 3: how to take an accurate measurement.* Nursing Times. Available at:

https://www.nursingtimes.net/clinical-archive/respiratory-clinical-archive/respiratory-rate-3-how-to-take-an-accurate-measurement-25-06-2018/ (Accessed: 01/28/2021).

Wilkinson, J. N. and Thanawala, V. U. (2009). "Thoracic impedance monitoring of respiratory rate during sedation – is it safe?" *Anaesthesia* 64.4. Publisher: John Wiley & Sons, Incorporated, pp. 455–456. ISSN: 0003-2409. DOI: 10.1111/j.1365-2044.2009.05908.x.

Wong, J., Goh, Q. Y., Tan, Z., Lie, S. A., Tay, Y. C., Ng, S. Y., and Soh, C. R. (2020). "Preparing for a COVID-19 pandemic: a review of operating room outbreak response measures in a large tertiary hospital in Singapore". *Canadian Journal of Anesthesia/Journal canadien d'anesthésie* 67.6, pp. 732–745. ISSN: 1496-8975. DOI: 10.1007/s12630-020-01620-9.